Faculty of Natural Science and Technology
Department of Physics

MASTER'S THESIS FOR

STUD. TECHN. JON HOLMESTAD

Thesis started: 19.01.2009
Thesis submitted: 15.06.2009

DISCIPLINE: MATERIALS PHYSICS

Norsk tittel: *Høytemperaturstabilitet i Al-Mg-Si-legeringer*

English title: *High-Temperature Stability of Al-Mg-Si alloys*

This work has been carried out at the Department of Physics under the supervision of Research Scientist Calin Marioara, SINTEF Materials and Chemistry and Professor Randi Holmestad, NTNU.

Trondheim, 15. June 2009

Randi Holmestad

Responsible supervisor

Professor at Department of Physics

Abstract

This Master thesis investigates the high-temperature stability of five age-hardenable Al-Mg-Si-Cu alloys and which metastable phases have formed during the heat treatment. These metastable phases are responsible for the strengthening increment of the alloys during ageing. Three alloys were also investigated to find the equilibrium phase.

The alloys investigated all have 0.27 atomic percent manganese and 0.10 atomic percent iron. The copper content varies between 0.11 and 0.17 atomic percent. KK11 have an effectige Mg/Si-ratio of 1.50, KK13 of 3.00. KK1, KK14, KK15 and KKAg all have an effective Mg/Si-ratio of 2.00. KKAg has an addition of 0.03 atomic percent silver.

All the alloys except KK1 were first treated to the T6-condition of peak hardness before any Vickers hardness measurements were done. The Vickers hardness was then tested until the ageing had lasted a total of 100 hours at $250°C$. The intervals between measurements were short in the beginning, longer near the end.

KK14 and KKAg have the highest peak hardness, while KK11, KK13 and KK15 are slightly weaker. KK11 and KK15 remains the weakest alloys during the entire ageing process, while KK13 retains hardness the best and ends with the highest hardness. The hardness of both KK14 and KKAg drop off quicker than for KK13 and from 2 hours until the end, KK13 has the highest hardness.

KK1, KK13 and KKAg were also aged at $350°C$ for 5 hours to investigate what is probably the equilibrium phase. The hardness measurement showed that the hardness was the same, approximately 50 for all three alloys.

KK13 and KKAg were investigated by Transmission Electron Microscopy after the first ageing process. It was found that KK13 had a higher number density of precipitates ($1181\ \mu m^{-3}$), shorter ($240.2\ nm$) and finer ($30.8\ nm^2$) needles than KKAg. KKAg has number density of $477\ \mu m^{-3}$, needle length of $410.3\ nm$ and cross-sections of $69.5\ nm^2$. Some high-resolution transmission electron microscopy was used to identify the phases that formed.

KK13 has mainly platelike precipitates oriented along the $\langle 100 \rangle$-direction of aluminium. A few Q'-precipitates oriented along $\langle 510 \rangle$ were also observed. In the KKAg alloy, both types of precipitates are observed, but a higher amount of transformation to

the Q-type precipitate was observed.

After the high-temperature ageing, the alloys were qualitatively investigated. The microstructure looked similar and the high-resolution images of the precipitates indicate that they are mainly Q-type precipitates.

One dispersoid was investigated using XEDS and diffraction to determine the phase in the KK1 alloy. It seems to be of the $Al_{97-105}(Fe+Mn)_{23-24}Si_{5-11}$-phase with a cubic unit cell with $a = 1.256\ nm$.

Preface

This Master's thesis is the result of my work at the department of Physics at the Norwegian University of Science and technology. The heat treatment and the hardness testing were performed at the department of Materials Technology. This work is a continuation of my project work and therefore one section has been used for a brief summary of this.

I would like to thank my supervisors, Professor Randi Holmestad of the department of Physics at NTNU and research scientist Calin D. Marioara from SINTEF Materials and Chemistry for all their guidance, and also help to get good TEM pictures. Also, I would like to thank PhD-student Ruben Bjørge for explaining and showing how to do hardness testing and TEM specimen preparation. I would also like to thank Bjørn G. Soleim and Ton Van Helvoort for their work of making the microscopes working as much as possible. Also, thank to Jostein Røyset, researcher at Norsk Hydro, for reading and suggesting corrections of this thesis. I would also like to thank my girlfriend, Johanne Vikin for being supporting and understanding during the last hard weeks before the deadline.

Trondheim, 04.06.2009

Jon Holmestad

Alloy compositions in atomic percentage.

Alloy	Si	Mg	Cu	Fe	Mn	Ag
KK1 at%	0.62	1.00	0.17	0.10	0.27	-
KK2 at%	0.53	1.00	0.17	0.10	0.04	-
KK3 at%	0.87	0.75	0.11	0.10	0.27	-
KK4 at%	0.95	0.67	0.22	0.10	0.27	-
KK11 at%	0.72	0.91	0.17	0.10	0.27	-
KK13 at%	0.50	1.13	0.17	0.10	0.27	-
KK14 at%	0.67	1.10	0.11	0.10	0.27	-
KK15 at%	0.57	0.90	0.15	0.10	0.27	-
KKAg at%	0.62	1.00	0.14	0.10	0.27	0.03

Contents

CHAPTER 1

Introduction

Aluminium is the most common metal in the earths crust, but is very rare in its pure form. Aluminium alloys are becoming more common in more and more applications due to its low weight and good resistance to corrosion[**1**]. It was found in 1906 that the hardness of aluminium alloys increased after heat treatment, but not until the electron microscope was built in the 1950s the reasons for this was discovered[**2**]. The small particles of metastable phase that precipitates were not possible to see using light microscopes. These metastable phases cause the strengthening of the alloy by preventing dislocation motion. In the years after this, many new age-hardenable alloys have been developed.

This Master thesis is a part of a project run by Norsk Hydro, SINTEF, NTNU and Steertec Raufoss to investigate the high-temperature stability of aluminium alloys for use in the car industry. The problem with aluminium is that the precipitates form at low temperatures. This means, that as cars become more compact, the temperature in the engine and parts close to the engine will increase. If aluminium is going to replace steel in this area, an alloy that retains a high strength after repeated heating has to be discovered. For this, it is also important to develop an aluminium alloy with the strength as close to steel as possible. The requirement set by Steertec AS was that the hardness is above 100 HV 5 after 100 hours of heat treatment at 250 ° C.

Aluminium has a much lower density than steel, meaning that car parts made of aluminium will be lighter than steel even if they must be constructed somewhat bulkier to keep the same strength. The lower weight of the car will lead to lower fuel consumption and lower emission of climate gases into the atmosphere.

The aluminium industry is an important part of the Norwegian economy, in 2007 about 5 % of the total Norwegian export, oil industry included, was products from the aluminium industry[**3, 4**].

The intention of this Master's thesis was to discover which of the investigated alloys retained the hardness for the longest time. Then investigate which precipitates have formed and try to explain the hardness differences by this. All the alloys went through one of the heat treatments, first to peak hardness, then ageing for 100 hours at $250°C$.

Another intention of this thesis was to investigate what the equilibrium phase of these alloys were. They were submitted to 5 hours at $350°C$, hardness tested and investigated

in the TEM.

Chapter 2 explains the theory needed for understanding the experiments performed, chapter 3 tells all about how the experiments were performed. In chapter 4, a brief summary of my project work is given. This thesis is a continuation of this work. In addition, the results are shown and discussed. Some further work is also suggested in this chapter. The conclusions of this work are given in chapter 5, while a table and all the images used for measurements are given in appendix A and B.

CHAPTER 2

Theory

2.1. Crystal systems

A crystal is a spatially periodic structure, a structure with translational symmetry. This repeating structure is called the unit cell. The unit cell is a parallelepiped defined by the basis vectors $\mathbf{a_1}$, $\mathbf{a_2}$ and $\mathbf{a_3}$. Each atom in the crystal have a position given by the vector:

$$\mathbf{R_{uvw}} = u\mathbf{a_1} + v\mathbf{a_2} + w\mathbf{a_3} \tag{2.1}$$

Where u, v and w are integers.

There are 7 different crystal systems each defined by different lengths of the basis vectors and the angle between them. The crystal systems are triclinic, monoclinic, orthorhombic, tetragonal, rhombohedral(trigonal), hexagonal and cubic. In some crystals there is more than one equivalent lattice point. Lattice points are equivalent when their geometric surroundings in all respects are identically alike[**5**]. These points are called Bravais lattice points and for most crystal systems, it is possible to find two or more of these points. The lattice is then called a Bravais lattice and they are shown in figure 2.1. The possibilities are primitive (1 Bravais point), end/side/base-centered (2 Bravais points), body-centered (2 Bravais points) and face-centered (4 Bravais points).

A symmetry operation is an operation after which the unit cell is superimposed on itself. Possible symmetry operations in addition to translation are rotations and reflections and combinations of these. Possible rotations compatible with translational symmetry are two-fold, three-fold, four-fold and six-fold rotations. The group consisting of all possible symmetry operations of a unit cell is called a point group and there are 32 different point groups.

In addition, glide planes and screw axis are possible operations giving the total number of possible space groups as 230. A glide plane is a combination of translation and reflection, whereas a screw axis is translation and rotation. These are shown in figure 2.2.

Lattice planes are given by the Miller indices h, k and l which are the reciprocal of the respective integers u, v and w given above. It is denoted as (hkl). The most important planes in the cubic crystal system is given in figure 2.3. A set of all the equal planes, i.e (100), (010) and (001) is denoted $\{100\}$[**7**].

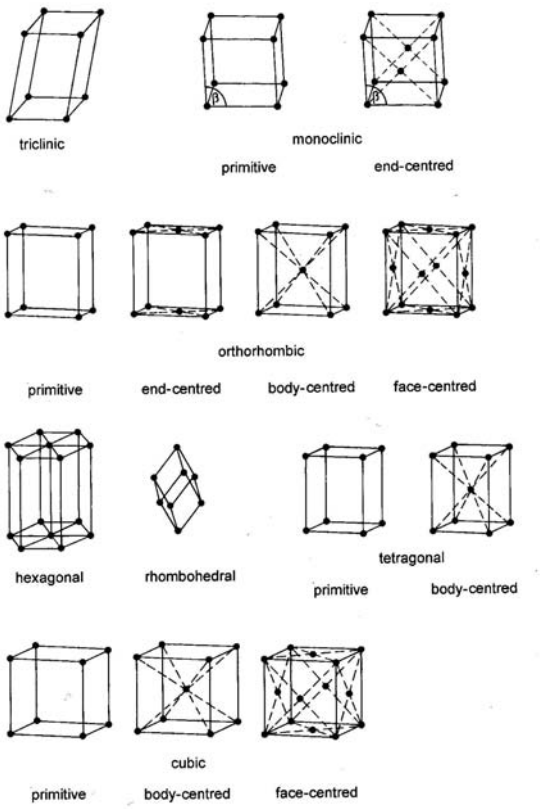

FIGURE 2.1. The 14 different Bravais lattices[**6**].

The lattice direction is given by $[uvw]$. In the cubic crystal system, the [100] is along the edge of the cube, the [110] along the diagonal on one of the sides of the cube and the [111] is the body diagonal of the cube. The set of all equal directions are written as $\langle 100 \rangle$[**7**].

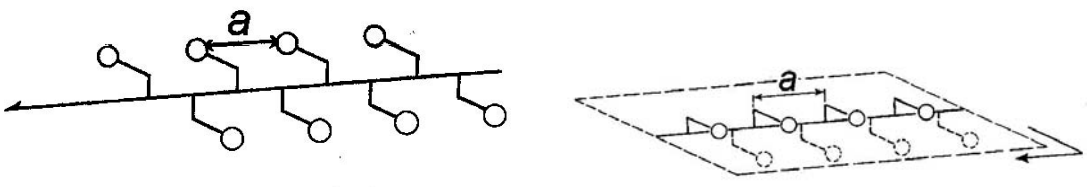

(a) (b)

FIGURE 2.2. (a) An illustration of a screw operation[**6**], (b) An illustration of a glide plane[**6**].

A zone axis, denoted $[UVW]$, is a common direction for all the planes in the zone[**8**].

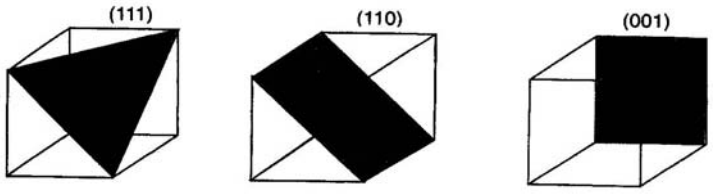

FIGURE 2.3. The (111), (110) and (100) planes in a cubic crystal system[**7**].

2.2. Dislocations

In real life, a perfect crystal does not exist, there are always some defects. Point defects are defects only consisting of one atom, but they can also appear in pairs called "Frenkel defects". At any finite temperature, there is always a probability that an atom will jump from its lattice site. This is of the form $\exp(-E_a/k_BT)$ where E_a is an activation energy, k_B is Boltzmann's constant and T is the temperature in Kelvin. The atom can jump to a vacant lattice site, moving the vacancy through the lattice or it can jump to an interstitial site. There can also be impurity atoms in the lattice. These point defects are one-dimensional defects. Different point defects are shown in figure 2.4(a).

Dislocations are extended regions of lattice defects, called two-dimensional defects. There are two types, edge dislocations and screw dislocations. An edge dislocation can be visualized as an extra half-plane of atoms in the lattice[**2**] as shown in figure 2.4(b). A screw dislocation is visualized in figure 2.4(c). The Burgers vector is defined as the vector needed to close a loop moving from atom to atom. If no dislocations are present in the loop, there will be the same number of steps in each direction, but this is not possible if a dislocation is located within the loop. For an edge dislocation, the Burgers vector is perpendicular to the dislocation line while it is parallel with the dislocation line for a screw dislocation[**2**]. Dislocations can also be a combination of edge- and screw-dislocations.

The strength and ductility of the metals are mostly controlled by the dislocations because this is where slip is most likely to occur. Heat treated metals have a dislocation density of $10^7\ cm^2$[**2**] and preventing the movement of these dislocations will make the material stronger. The slip direction is always in the direction of closest packing, so in a fcc-crystal, slip is most likely to occur when the dislocation has a Burgers vector of[**2**]:

$$b = \frac{a}{2}\langle 110\rangle \tag{2.2}$$

The closest packed plane, e.g. the slip plane, in a fcc-crystal is the $\{111\}$-plane.

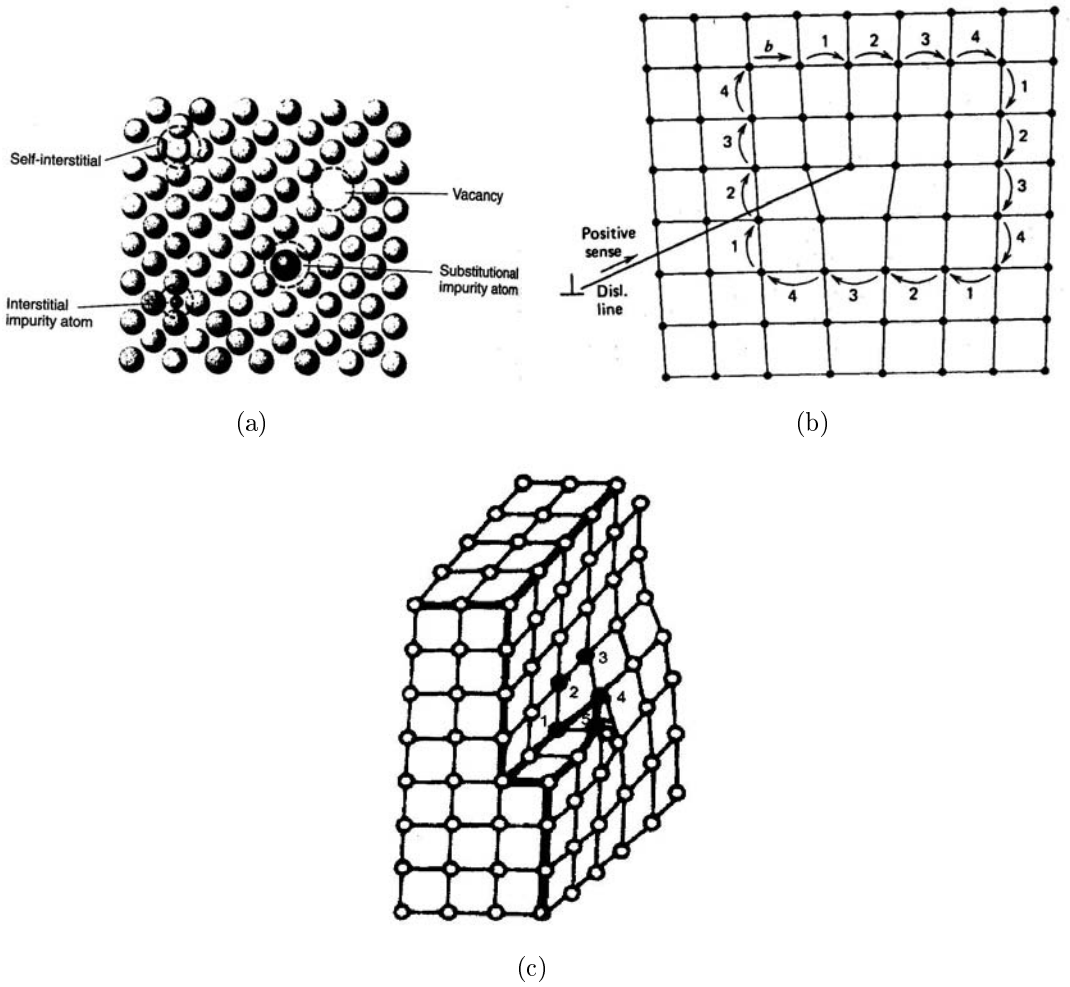

FIGURE 2.4. (a) The most normal point defects in a lattice[**7**], (b) an edge dislocation and its Burgers vector[**2**], (c) a screw dislocation and its Burgers circuit[**7**].

2.3. Lattice strain

The coherency of a particle depends on whether it has the same crystal structure as the parent matrix. Coherency is a measure of the fit between the lattice planes in the parent matrix and the lattice planes in the precipitate[**9**]. In a coherent particle, the lattice planes are continuous through both the matrix and the precipitate. If the spacing of the lattice planes are the same in both the precipitate and the matrix, the particle is said to be fully coherent as shown in figure 2.5(a). If the spacing between lattice planes is not equal, lattice planes can be bent so they match at the interface. It is usually the lattice planes in the matrix that bend and form a strain field around the precipitate as shown in figure 2.5(b). Strain fields hinder the movement of dislocations, so this increases the hardness of the material. Both fully coherent and coherent particles have a low surface

energy and they form at low temperatures.

A partially coherent particle, as shown in figure 2.5(c) usually has one coherent and one incoherent interface with the matrix. The lattice spacing across the coherent interface can be identical or different. If they are different, a strain field arises here just as for the coherent particle. Partially coherent particles give rise to dislocations at the incoherent interface, which increases the surface energy of the particle. The strain field of the particle weakens, as the particle is no longer coherent in all directions. The partially coherent particles need a higher temperature than the coherent particles to form.

The crystal structure of a incoherent particle is completely different from the matrix as shown in figure 5(d) and here, no strain field arises. Incoherent interfaces are similar to high-angle grain boundaries and the dislocations glide along the interface and the material weakens. The interface energy of these particles is large, and they only form at relatively high temperatures. The temperature stability is shown in figure 2.10 and more closely explained in section 2.7.

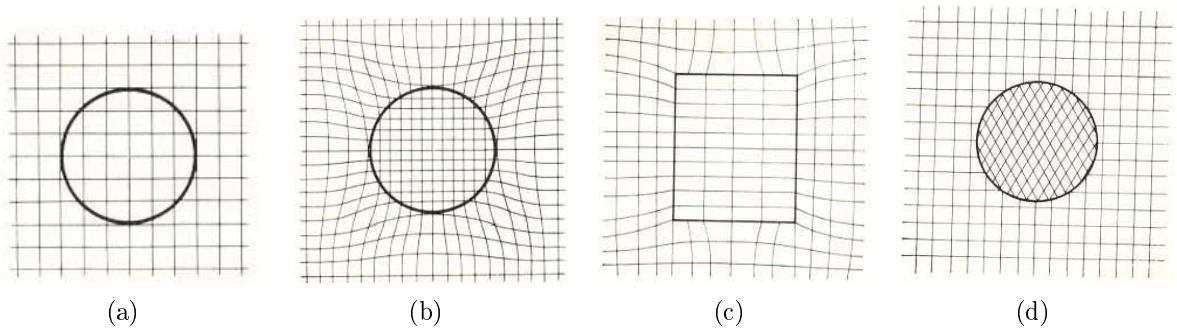

FIGURE 2.5. (a) Fully coherent particle[**9**], (b) Coherent particle[**9**], (c) Partially coherent particle[**9**], (d) Non-coherent particle[**9**].

2.4. Nucleation

There are two possible ways of nucleation, homogeneous and heterogeneous. Homogeneous nucleation means that the new phase forms uniformly in the parent phase, while heterogeneous nucleation means that the new phase forms primarily at inhomogenities like dislocations, grain boundaries and impurities in the parent phase. All phase transformations involves a structure change, but they can also involve a composition change and/or strain formation[**2**].

For a phase transformation to occur, the free energy change has to be negative, i.e. $\Delta G < 0$. The nucleation is inhibited by the particle/matrix surface energy, strain energy due to different lattice parameters in the lattice and the precipitate and the bulk free energy change. The relationship between these for homogeneous nucleation are[**2**]:

$$\Delta G = n\Delta G_B + \eta n^{2/3}\gamma + nE_s \tag{2.3}$$

Where:

n: Number of atoms in the nucleus
ΔG_B**:** $\frac{G_{nucleus}-G_{matrix}}{n}$ = bulk free energy change per atom
η**:** shape factor such that $\eta n^{2/3}$ = surface area
γ**:** surface tension = surface free energy
E_s**:** strain energy per atom in the nucleus

ΔG_B will be negative below the temperature of the phase transformation, while both E_s and γ are positive. A plot of the change in free energy as a function of nucleus size is shown in figure 2.6. As can be seen from equation 2.3, ΔG_B has to be negative and have a larger absolute value than E_s for nucleation to occur.

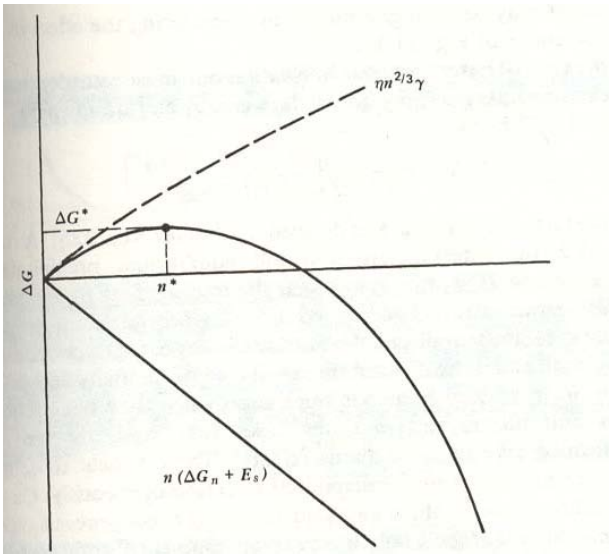

FIGURE 2.6. Free energy of formation as a function of nucleus size[**2**].

As can be seen in figure 2.6, at a critical nucleus size n*, the free energy of formation is lowered upon the addition of more atoms to the nucleus. Assuming everything but the nucleus size as constant, this gives the free energy change at the critical size as[**2**]:

$$\Delta G^* = \frac{4}{27}\frac{\eta^3\gamma^3}{(\Delta G_B + E_s)^2} \tag{2.4}$$

For heteregeneous nucleation, the effect of the nucleation interface on the surface energy and the strain energy must be taken into account. This gives the critical free energy change for heterogeneous nucleation as[**2**]:

$$\Delta G^* = \frac{4}{27}\frac{\eta^3\gamma^3}{(\Delta G_B + E_s)^2}\left[\frac{2-3S+S^3}{4}\right] \tag{2.5}$$

where $S = \sin\delta$. δ is the dihedral angle, e.g. the angle between the precipitate grain boundaries at the triple point. A normal precipitation sequence for age-hardenable alloys is shown in table 2.1.

TABLE 2.1. Precipitation sequence normally observed in age-hardenable alloys[**2**].

Precipitate	Crystal structure	Coherency	Nucleation
GP Zones	Same as matrix	Fully coherent	Uniform $10^{18}/cm^3$
Intermediate	Different from matrix	Fully or partially coherent	Heterogeneous
Equilibrium	Different from matrix	Noncoherent	Heterogeneous

2.5. Aluminium alloys

Aluminium is the most common metallic element in the crust of the earth. It contains about 8% of Aluminium. The only problem is that Aluminium has a strong affinity for Oxygen, so it is rarely found in its pure state. Most of the Aluminium produced is from bauxite ore ($AlO_x(OH)_{3-2x}$). Aluminium in its pure form is soft and has a low melting temperature, approximately 660°[**10**]. It is very light, only $2.7g/cm^3$, which makes it very attractive for applications where weight is a concern. The density is only 1/3 of the density of steel, and this changes little when alloying elements is added, but the strength increases significantly. The most used alloying elements are Magnesium (Mg), Silicon (Si), Copper (Cu), Manganese (Mn) and Zinc (Zn).

There is an international classification of wrought Aluminium Alloys called The International Alloy Designation System where each alloy is given a 4 digit number where the first number tells the major alloying elements. The classification is as follows[**1**]:

1xxx: Alloys containing at least 99.00% Al
2xxx: Al-Cu alloys
3xxx: Al-Mn alloys
4xxx: Al-Si alloys
5xxx: Al-Mg alloys
6xxx: Al-Mg-Si alloys
7xxx: Al-Zn alloys
8xxx: Other alloying elements

In this project work, four different 6xxx-alloys were studied with hardness measurements. These alloys are commonly used in the automotive industry, as construction materials and for sports and recreational equipment. 6xxx-alloys have a good weldability, corrosion resistance and immunity to stress-corrosion cracking[**1**].

2.6. Hardening mechanisms

The increased strength of age-hardening alloys is due to the interaction between the precipitates and dislocations. The two most important interactions are called particle looping (Figure 2.7(a)) and cutting (Figure 2.7(b)).

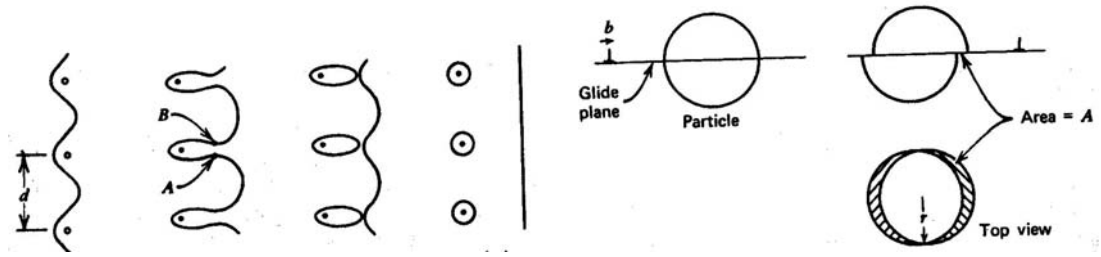

(a) (b)

FIGURE 2.7. (a) Particle looping[**2**], (b) Particle cutting[**2**].

In figure 2.7(a) the basic idea of particle looping is shown. The dislocations will bow out at the points where it meets a precipitate particle. As the stress increases, the points A and B in the figure meet. The dislocations at these points have different signs and will annihilate each other, creating a dislocation loop around the particle. The dislocation will continue past the particles as shown in the last drawing in figure 2.7(a). The increase in the critical resolved shear stress for particle looping is given as[**2**]:

$$\Delta\tau = (const)\frac{Gbf^{1/2}}{r}\ln\frac{2r}{r_0} \tag{2.6}$$

Where:

$\Delta\tau$: The increase in critical resolved shear stress.
const: Is 0.093 for edge dislocations, 0.14 for screw dislocations.
G: The shear modulus[**6**].
b: Burgers vector of the dislocation.
f: Volume fraction of the precipitates.
r: The particle radius.
r_0: Small radius inside of which Hooke's law fails[**2**].

If the repulsive force between the particle and the dislocation is not large enough, the particle will be cut, not looped. If the dislocation is able to move right through the particle, a part of the particle will be offset by one Burgers vector in relation to the other part as shown in figure 2.7(b).

There are two different interactions for particle cutting, short-range interaction (less than $10 \cdot b$) and long-range interactions at longer distances. An ordered particle that is cut will create an antiphase boundary which has a high surface energy, γ_A[**2**]. This increases

the shear stress required by[**2**]:

$$\Delta\tau = 0.28\frac{\gamma_A^{3/2} f^{1/3}}{\sqrt{G}b^2} r^{1/2} \tag{2.7}$$

The cutting also increases the surface area of the precipitate, causing an increase in the surface energy given by[**2**]:

$$\Delta\tau = \frac{1.1}{\sqrt{\alpha}}\frac{\gamma_s^{3/2} f^{1/2}}{Gb^2} r^{1/2} \tag{2.8}$$

Where α is a function of the dislocation line tension and γ_s is the surface energy of the precipitate. A long-range interaction is the interaction between the dislocation strain field and the particle strain field. This is given by[**2**]:

$$\Delta\tau = \left[\frac{27.4E^3\epsilon^3 b}{\pi T(1+\nu)^3}\right]^{1/2} f^{5/6} r^{1/2} \tag{2.9}$$

where

E: Young's modulus

ϵ**:** A function of the disregistry δ, i.e. the mismatch between the particle lattice and the matrix.

T: The line tension.

ν**:** Poisson's ratio.

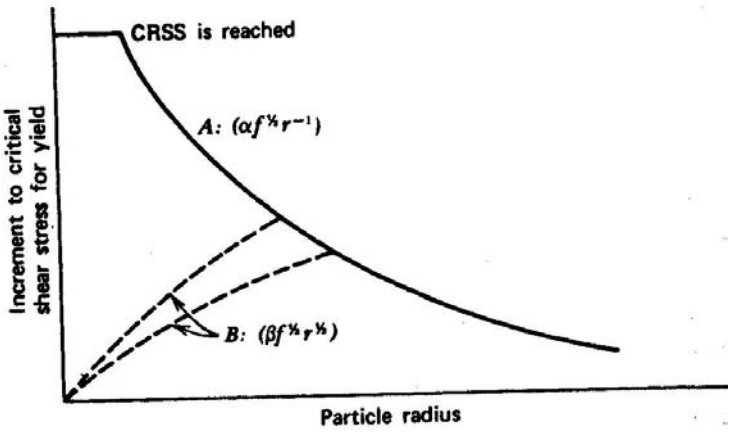

FIGURE 2.8. Strengthening increment versus particle size[**2**].

As can be seen from equations 2.7, 2.8 and 2.9, the increased in shear stress follows the form $\beta f^x r^{1/2}$ where β and x depends on the main interaction. Particle looping gives a higher increase in yield stress for small particles than particle cutting, and will therefore only happen when the particles are large and no longer can be cut. A plot of this can be seen in figure 2.8 where curve A is for particle looping and curve B is for particle cutting.

2.7. Precipitation sequence

2.7.1. General precipitation sequence. The top of figure 2.9 shows a phase diagram, let us consider an alloy consisting of x_0 of B and $(1 - x_0)$ of A. As the temperature lowers, precipitates will start to form in the α-phase. The change will be:

$$\alpha(x_0^0) \rightarrow \alpha(x_0^\alpha) + \beta(x_0^\beta)$$

If the temperature is lowered fast, e.g. water quenching, no precipitates will form, but you will get a super saturated solid solution (SSSS). This means that all of the B-particles are dissolved in the α-matrix. This is not stable, and as shown in figure 2.9 a new phase will immediately start to form. If the temperature is lowered enough, i.e. to T_L in figure 2.9, the equilibrium phase will not start to form immediately. Either GP-zones or an intermediate phase will form at first, because they are coherent or partially coherent and have a lower surface energy. Figure 2.9 shows that at the low temperature all the precipitates have a negative change in free energy, so all may form. The intermediate metastable phases will form quickly due to the low surface energy.

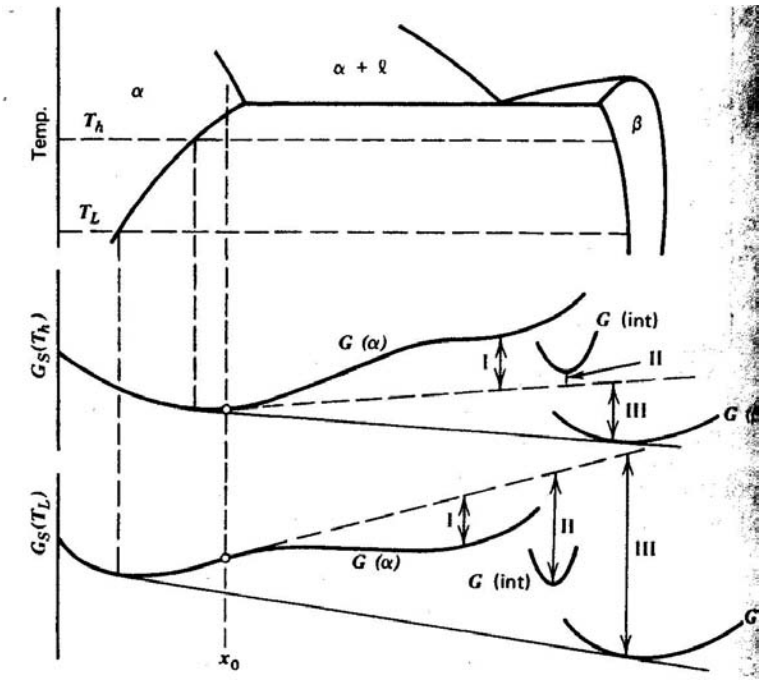

FIGURE 2.9. Illustration showing the free energy of formation of GP-zones(I), intermediate precipitates (II) and equilibrium precipitates (III) at two different temperatures[**2**].

Figure 2.10 shows a metastable phase diagram where the stability of the GP-zones and the intermediate precipitates is shown.

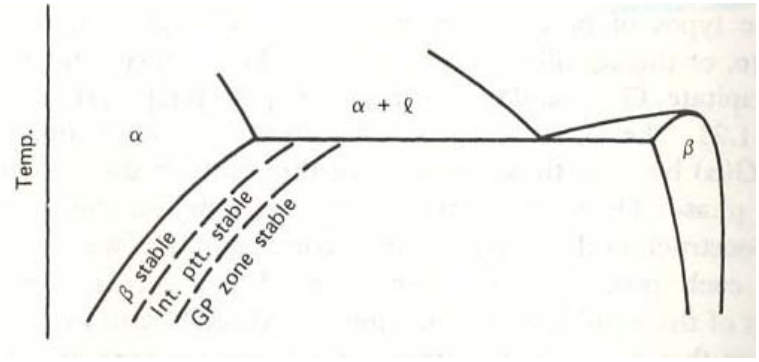

FIGURE 2.10. A metastable phase diagram[**2**].

Normally, an alloy is water quenched to room temperature and then reheated to a low temperature so that the wanted metastable phases may form. It is usually these metastable phases that cause the increase in strength in age-hardenable alloys.

A general precipitation sequence can be:

$$SSSS \rightarrow GP - zones \rightarrow Intermediate\ phase(s) \rightarrow Equilibrium\ phase$$

Table 2.1 states whether the different phases usually are coherent or incoherent with the parent matrix.

2.7.2. Precipitation sequence in Al-Mg-Si-Cu alloys. The precipitation sequence for an Al-Mg-Si-Cu alloy is as follows[**11**]:

$$SSSS \rightarrow atomic\ cluster \rightarrow GP - zones \rightarrow \beta'',\ L,\ C, S, QP,\ QC \rightarrow Q' \rightarrow Q$$

The main strengthening of these alloys occur when the metastable phases β'', L, C, S, QP or QC are formed[**11**].

The Supersaturated solid solution is obtained by quenching the alloy quickly from a temperature below the solvus line for aluminium. When the alloy is rapidly cooled, all the alloying elements are frozen into the material and a much higher concentration of vacancies than the equilibrium concentration at room temperature[**2**].

During storage at room temperate, the atomic clusters start to form. Due to a higher solubility of Mg in Al, Si leaves the solution and forms clusters. This nucleation of Si-clusters will occur down to $-50°$ C[**12**], below which vacancy movement is low. Heating above $-50°$ C will cause the Mg-atoms to migrate towards the clusters and the Mg/Si-ratio in the clusters increases with time when heated to 70° C[**12**]. The number of atomic clusters that is formed is important for the precipitation of the GP-zones, so this storing time at low temperature is important for the material properties. All the precipitates discussed below are summarized in table 2.2. In addition, information about shape, lattice

parameters, space group and composition is given.

TABLE 2.2. Known precipitation phases in Al-Mg-Si-Cu alloys[**11**].

Phase	**Shape**	**Composition**	**Space group**	**Lattice parameters** (nm)
GP-zones	Needle	$Mg_{2+x}Al_{7-x-y}Si_{2+y}$ $1 < x + y < 3$	C2/m	$a = 1.48$ $b = 0.405$ $c = 0.648$ $\beta = 105.3°$
β''	Needle	Mg_5Si_6	C2/m	$a = 1.516$ $b = 0.405$ $c = 0.674$ $\beta = 105.3°$
L	Needle	Unknown	Unknown	Unknown
QP	Needle	Unknown	Hexagonal	$a = b = 0.393$ $c = 0.405$
QC	Needle	Unknown	Hexagonal	$a = b = 0.670$ $c = 0.405$
S	Needle	Unknown	Hexagonal	$a = b = 0.7$ $c = 0.405$
Q'	Needle	$Al_3Cu_2Mg_9Si_7$	$P\bar{6}$	$a = b = 1.032$ $c = 0.405$ $\gamma = 120°$
Q	Needle	$Al_3Cu_2Mg_9Si_7$	$P\bar{6}$	$a = b = 1.039$ $c = 0.402$ $\gamma = 120°$
C	Plate	$Al_2Mg_8Si_6Cu_2$	$P2_1/m$	$a = 1.032$ $b = 0.81$ $c = 0.405$ $\gamma = 100.9°$

The GP-zones are the first phase to form on the atomic clusters. These zones are fully coherent with the aluminium matrix[**12**] and have a monoclinic unit cell. These GP-zones are very small, a size of $1-3\ nm$[**12**]. They are stable at 100° C[**13**]. The high coherency with the matrix means that it only has a low strain field and it is not this precipitate that gives the highest hardness. The particle density of these GP-zones is very high.

The β"-phase forms from the GP-zones at temperatures above 125° C[**13**]. This phase is also monoclinic, but is less coherent than the GP-zones. It is only fully coherent with the Al-matrix along the b-axis[**12**]. This causes an increased strain field, and the β" is the main strengthening particle in Al-Mg-Si alloys[**14**]. These particles form on the GP-zones and it is due to the coherency and strain fields that inhibit dislocation motion that the

strengthening occurs. In Al-Mg-Si-Cu alloys with low copper content, more β"-phase will form, but it is not the main hardening phase[**11**].

The L-phase is assumed to be a disordered C-phase[**11**]. The C-phase is called the plate phase and this phase has a monoclinic unit cell with coherency with the matrix only in the c-direction. The composition is assumed to be $Al_2Mg_8Si_6Cu_2$[**15**] and a probable unit cell is given in figure 2.11(a)

The S-phase are needles oriented along $\langle 510 \rangle$ Al or $\langle 110 \rangle$ Al. Some of these precipitates have regions of hexagonal symmetry which may suggest that it is a disordered QC-phase[**11**].

Both QP and QC have hexagonal unit cells, and the QC-phase is the ordered version of the S-phase. The QC-phase is oriented in a similar direction to the L-phase, but no hexagonal unit cells have been found in the L-phase to determine whether the L-phase is a disordered QC-phase[**11**].

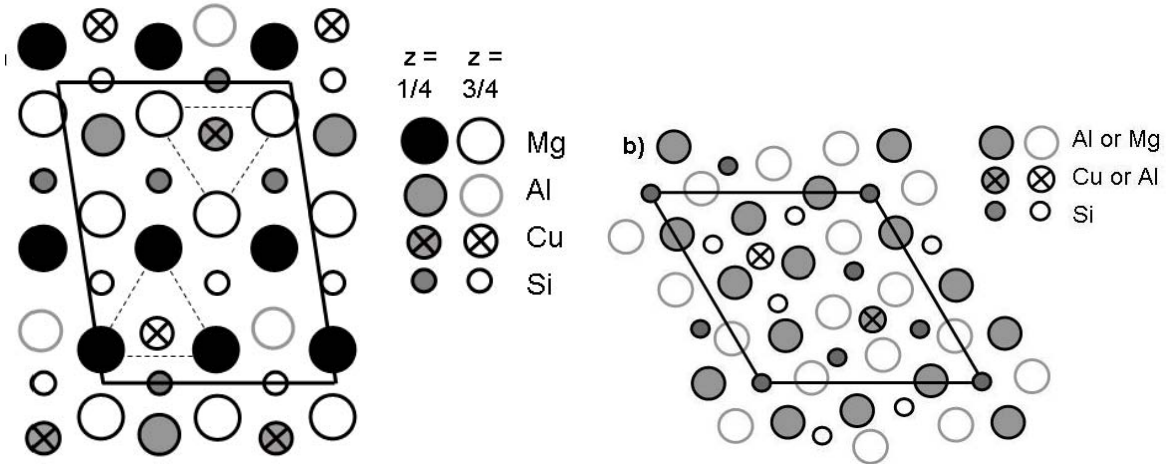

FIGURE 2.11. (a) The probable unit cell of a C-type precipitate, (b) The unit cell of a Q'-precipitate[**15**].

Q' is the phase that forms in overaged samples with an hexagonal unit cell given in figure 2.11(b). It is only assumed to have the same composition as the equilibrium phase Q, but with a slightly more coherent unit cell[**15**] in the c-direction causing more strain and a higher hardening effect.

The Q-phase is probably the equilibrium phase, this is partially coherent with the Al-matrix and causes little hardening. This phase only occurs after long overaging at high temperatures.

2.7.2.1. *Addition of silver.* Few detailed studies of the crystal structure of the precipitates in Ag-containing Al-Mg-Si alloys have been made. It has been found that the addition of silver stimulates clustering of Si-Mg-Ag-vacancy cluster[**16**]. Silver is added because it shows increase of hardness and age-hardening[**17**].

It is usually assumed that the precipitates are the same as those in alloys without Ag addition. A precipitate with a crystal structure similar to that of Q' has been found[**18**]. This precipitate has a lattice constant $a = 1.05 \pm 0.01\ nm$ and is called Q_{Ag}. γ and c probably remains the same. The β' also has a similar unit cell with silver additions as without. The unit cell is only slightly smaller[**19**].

2.7.3. Dispersoid phases. The most common dispersoid phases found in Al-Mg-Si alloys are given in table 2.3. Which dispersoids that are formed vary both according to the alloy composition and the time of the heat treatment[**22**]. The dispersoids containing manganese has been shown to inhibit grain growth[**23**]. They also act as barriers to dislocation movement[**24**].

2.8. Vickers Hardness

The test for Vickers hardness is carried out by indenting the sample with a diamond pyramid tip with a top angle of 136° with a load of between 1 and 10 kg. This is shown in figure 2.12(a).

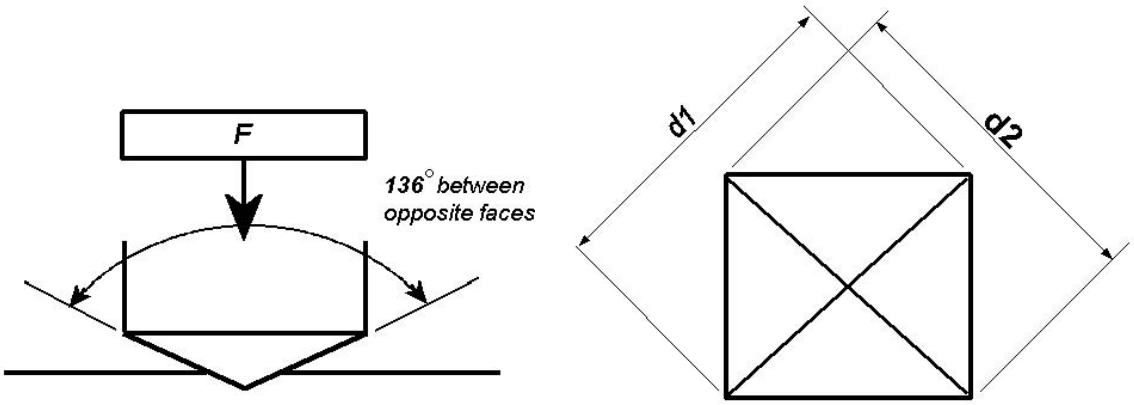

FIGURE 2.12. (a) Indenting of the sample, (b) How to measure the size of the indentation[**25**].

The diagonals (figure 2.12(b)) of the indentation is measured and the average, d, calculated. The Vickers hardness is then calculated using the formula below[**25**]:

$$HV = \frac{load}{surface\ area} = \frac{2F \sin \frac{136°}{2}}{d^2} = 1.8544 \frac{F}{d^2} \tag{2.10}$$

TABLE 2.3. Known dispersoid phases found in Al-Mg-Si alloys[**20, 21**].

Composition	**Space group**	**Lattice parameters** (nm)
$AlMnSi$	Simple Cubic	$a = 1.26$
$Al_{12}Fe_3Si$	Base-centered Cubic	$a = 1.26$
$Al_{10}Mn_3Si$	Hexagonal	$a = 0.751$
		$c = 0.775$
$AlFeMnSi$	Tetragonal	$a = 2.20$
		$c = 1.25$
$AlMnFeSi$	Tetragonal	$a = 1.02$
		$c = 2.04$
$Al_{97-105}(Fe + Mn)_{23-24}Si_{5-11}$	Cubic	$a = 1.256$
Al_4Mn	Hexagonal	$a = 2.84$
		$c = 1.24$
Al_4Mn	Orthorombic	$a = 0.6795$
		$b = 0.9343$
		$c = 1.3897$
$Al_{16}Mn$	Tetragonal	$a = 0.754$
		$c = 0.790$
$AlFeSi$	Orthorombic	$a = 0.45$
		$b = 0.50$
		$c = 2.04$
$AlFeSi$	Monoclinic	$a = 0.79$
		$b = 3.66$
		$c = 1.01$
		$\beta = 100°$
$AlFeSi$	Monoclinic	$a = b = 0.618$
		$c = 2.08$
		$\beta = 91°$
$Al_8FeMg_3Si_6$	Hexagonal	$a = 0.662$
		$c = 0.792$

It is important that the measurements are only carried out on smooth and even surfaces. They should be free from lubricants and the surface must permit a clear determination of the lengths of the diagonals.

2.9. TEM

A transmission electron microscope (TEM) works mainly just the same as a light microscope, only with electrons instead of light. Due to the shorter wavelength of electrons the resolution of an electron microscope is much higher. Light microscopes have in general a maximum resolution of $0.2\mu m$ while a good electron microscope can have a resolution about 0.1 nm. A schematic overview of a TEM is shown in figure 2.13. The beam paths

of two electron beams are sketched through the microscope. Because the lenses in a TEM are magnetic, they are easily adjusted by changing the current through the coils which changes the magnetic field in the lenses and makes it easy to switch between different modes of operation of the microscope, i.e. between imaging and diffraction.

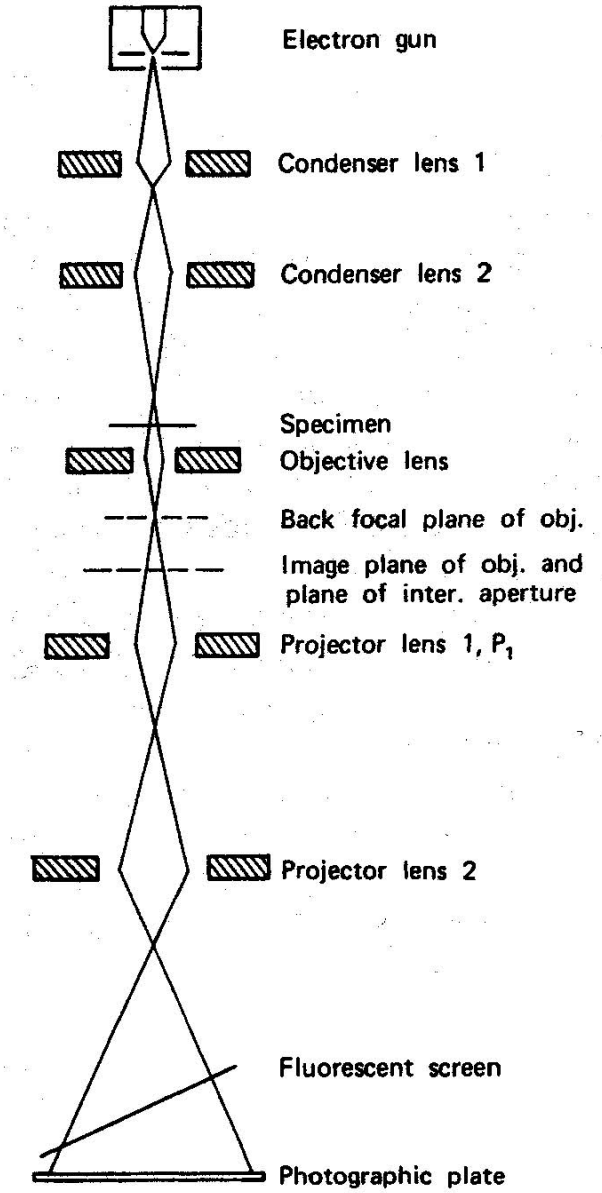

FIGURE 2.13. Schematic view of a TEM column[**2**].

Starting from the top, there are two different kinds of electron guns. They are thermionic source and field emission guns (FEG). There are two different thermionic sources, either tungsten (W) filament or a LaB_6-filament. Tungsten filaments have a higher energy spread, lower brightness and lifetime than LaB_6-filaments, but they require

a lower vacuum. A field emission gun has even better characteristics than a LaB_6-filament, but requires an even higher vacuum.

The next part is a system of condenser lenses which focuses the electron beam on the specimen and controls the size of the electron probe. Next is the specimen and since the electrons go through the specimen, TEM can only be performed on thin specimens. An objective lens forms the first intermediate image and diffraction pattern, only one of these is further magnified by the projector lenses. In the back focal plane of the objective lens there is also an aperture that can select one of the diffracted beams to produce dark field or bright field images. At last, the phosphor screen makes the electrons visible for the eye.

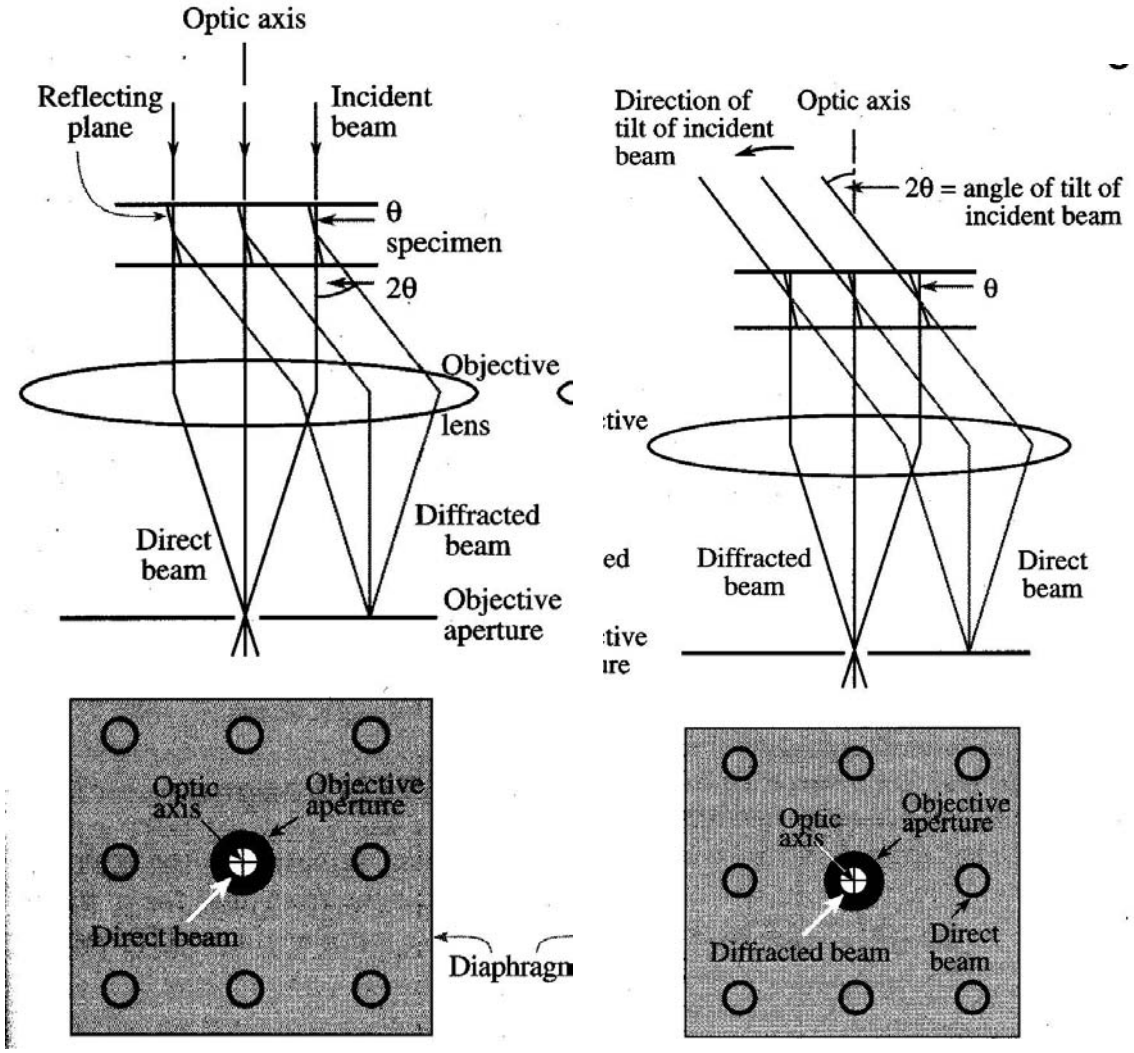

FIGURE 2.14. (a) Ray diagram for a bright field image with the area selected by the objective aperture., (b) Ray diagram for a dark field image with the diffraction spot selected by the objective aperture [8].

When an aperture is inserted in the back focal plane of the TEM, choosing only the direct beam in the diffraction pattern as shown in figure 2.14(a), it is called a bright field image. The Bragg-scattered electrons are not part of the image formed. A dark field image is formed by choosing one of the diffracted beams, but the incoming beam is slightly tilted before the sample so the diffracted beam is on-axis. This is shown in figure 2.14(b).

2.9.1. Electron scattering. A fraction of the electrons that hit the specimen will be scattered, most of these will be elastically scattered as shown in figure 2.15. The angle θ, called the Bragg angle, is half the angle between the incoming and the outgoing beam.

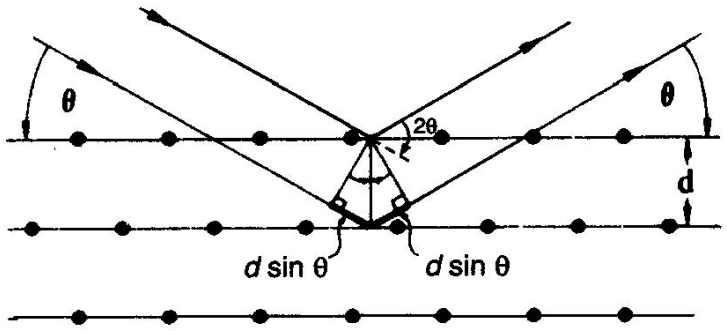

FIGURE 2.15. Bragg scattering from a crystal lattice[**7**].

The path difference between the two beams in figure 2.15 is $2d\sin\theta$. They will interfere according to Bragg's law:

$$2d\sin\theta = n\lambda \tag{2.11}$$

Where:

λ: The wavelength of the electrons.
d: The distance between lattice planes.
n: The order of reflection. If n is an integer, it is positive interference if $n = m+1/2$ it is called destructive interference.

2.9.2. Diffraction. For diffraction, the reciprocal lattice must be defined because Bragg diffraction of electrons by crystals occur when $\mathbf{Q} = \mathbf{g}$[**8**]. $\mathbf{g}$ is a reciprocal lattice vector. Bragg's law can be written as:

$$\frac{2\sin\theta}{\lambda} = \frac{n}{d} = |\mathbf{Q}| \tag{2.12}$$

Just like in real space, where a general lattice vector was defined in equation 2.1, we can define a general reciprocal lattice vector as:

$$\mathbf{g_{uvw}} = h\mathbf{a_1^*} + k\mathbf{a_2^*} + l\mathbf{a_3^*} \tag{2.13}$$

Where h, k and l are the Miller indices, $\mathbf{a_1^*}$, $\mathbf{a_2^*}$ and $\mathbf{a_3^*}$ are the reciprocal unit vectors. The reciprocal lattice vectors are given by $\mathbf{a_1^*} = \mathbf{a_2} \times \mathbf{a_3}/V_c$ where V_c is the volume of the unit cell.

An Ewalds sphere can be constructed to graphically show when some of the atoms in the lattice will diffract the electron beam, i.e. when one of the reciprocal lattice vectors equals the wave vector transfer, $\mathbf{Q}$. An Ewalds sphere is shown in figure 2.16. Here we can see that the wave vector transfer is equal to a reciprocal lattice vector and diffraction will occur.

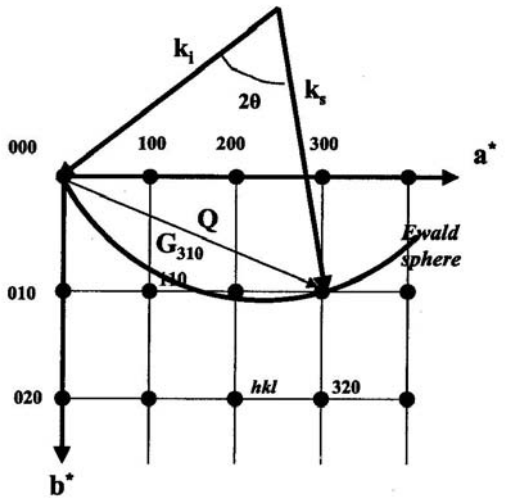

FIGURE 2.16. The Ewald sphere of a rectangular reciprocal lattice with a wave vector of the same magnitude as a lattice spacing [5].

The direct beam is defined as the 000-reflection where the sets of parallel hkl-reflections are an equal distance $1/d_{hkl}$ from the 000-reflection. Not all the reflections will be visible in all the different unit cells. This is due to extinction because the structure factor is zero for some reflections. The general structure factor can be written as[8]:

$$F(\mathbf{Q}) = \sum_i f_i e^{2\pi i(hx_i + ky_i + lz_i)} \tag{2.14}$$

Where the sum goes over all the atoms in the basis of the unit cell and f_i is the scattering factor. x_i, y_i *and* z_i are real lattice vectors. For a fcc-unit cell, as in aluminium,

the atoms are situated at $(0,0,0)$, $(1/2,1/2,0)$, $(1/2,0,1/2)$ and $(0,1/2,1/2)$. This gives the structure factor:

$$F = f(1 + e^{\pi i(h+k)} + e^{\pi i(h+l)} + e^{\pi i(k+l)}) \tag{2.15}$$

This means that only the reflections where h, k and l are either all even or all odd will give reflections for fcc-crystals like aluminium and a mixture of odd and even reflections will not give reflections.

2.9.3. X-ray generation. When high-energy electrons interact inelastically with the specimen, x-ray radiation can be created. This x-ray radiation can be created by two different mechanisms. The bremsstrahlung-radiation is created by a deceleration by the Coloumbfield of the nucleus. This results in x-ray radiation with energies up to the energy of the electron beam, E_0[8]. It is unlikely that all the energy of the electron will be lost in one interaction, so most likely the bremsstrahlung x-rays will have a lower energy, but still a continuous energy spectrum. The bremsstrahlung x-rays are highly anisotropic, mainly forward scattering. This anisotropy increases as the initial energy increases[8].

The most interesting x-ray radiation generated in the TEM is the characteristic x-rays. This radiation occurs when an incoming electron with a high enough energy, $E_0 > E_c$ knocks one of the inner shell electrons away from the atom. The electron escapes from the Coulomb-field of the nucleus. The atom is then in an excited state, and the easiest possibility to return to a lower energy state is by letting one of the electrons in an outer shell jump into the vacant position in the inner shell as shown in figure 2.17. This causes a reduction in energy for the atom and a photon with this energy is emitted[8]. The differences in energy between the different electron shells are characteristic of the different elements, hence characteristic x-rays are created.

2.9.4. XEDS. X-ray Energy Dispersive Spectroscopy measures the x-ray radiation created by the inelastically scattered electrons in the specimen. A typical spectrum is shown in figure 2.18. The energy is measured using a semiconductor detector that in theory measures the energy of each photon that enters the detector. The photon excites electrons into the conduction band and the total current is measured. By using XEDS, it is possible to determine which elements are present in the specimen. This is done by identifying the intensity peaks of the characteristic x-rays explained in section 2.9.3.

The peaks can be identified by their energy and the composition of the sample calculated using equation 2.16[8].

$$\frac{C_A}{C_B} = k_{AB}\frac{I_A}{I_B} \tag{2.16}$$

Where:

- C_A : Weight percent of element A.
- C_B : Weight percent of element B.

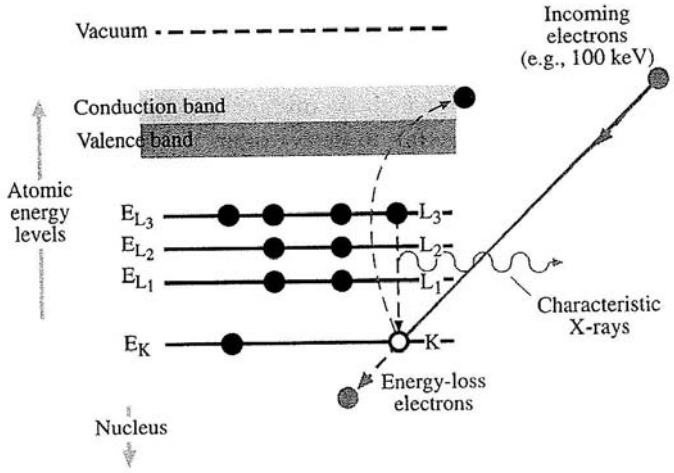

FIGURE 2.17. The mechanism for the creation of characteristic x-ray. An electron is knocked away from the K-shell while an electron from the L_3-shell fills this hole and emits a characteristic x-ray[8].

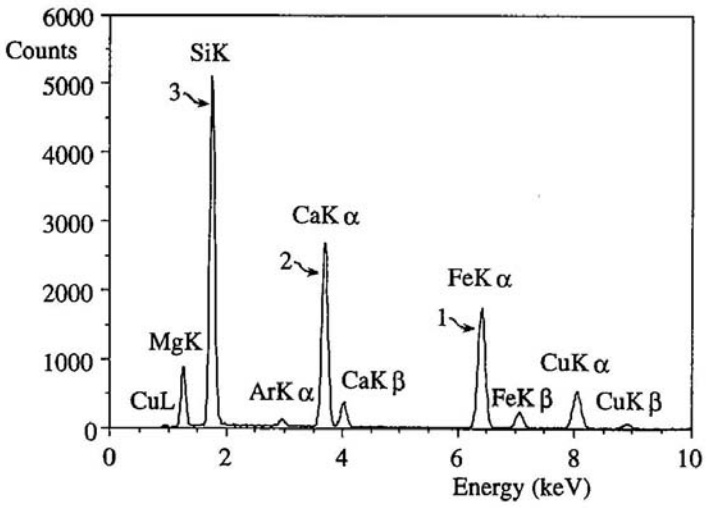

FIGURE 2.18. A typical XEDS-spectrum[8].

- k_{AB} : 'Constant' based on the system, accelrating voltage and atomic number of the elements.
- I_A : Number of counts in the A peak.
- I_B : Number of counts in the B peak.
- $C_A + C_b = 100\%$ for a binary specimen.

This equation can easily be extended for specimens containing more than two elements[8]. A problem in determining the elements in the specimen is that the microscope itself can create x-ray radiation when an electron hits a diaphragm, the sample holder or anything within the column. This means that the background radiation in the microscope must be

known before XEDS-analysis is performed.

2.9.5. (P)EELS. Parallel Electron Energy-Loss Spectrometry measures the energy of the electron after passing through the specimen. It graphically shows the electron loss after calibration of the zero-loss peak called I_0 in figure 2.19. After the electron beam goes through the column, a magnetic prism deflects the electrons toward the detector. The force, **F**, on the electron is given by Lorentz force law[**26**]:

$$\mathbf{F}_{mag} = Q(\mathbf{v} \times \mathbf{B}) \tag{2.17}$$

Where

Q: The charge of the electron.
v: The velocity vector of the electron.
B: The magnetic field.

This means that the electrons having lost less or no energy in the specimen will be less deflected than those having lost a lot of energy. All electrons having lost the same amount of energy is focused on the same diode, whether they are off-axis or on-axis entering the magnetic prism. In a (P)EELS, every diode counts the electrons during the entire integration time. A typical EELS-spectrum is shown in figure 2.19.

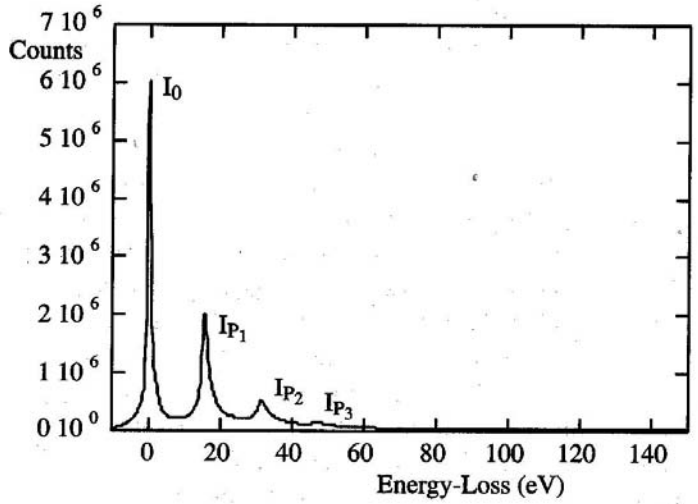

FIGURE 2.19. A typical EELS spectrum[**8**].

The I_0-peak consists of all the electrons that have passed through the sample without losing any energy at all, the next three peaks shown in the figure are the first to third plasmon peaks. Plasmons are the collective oscillations of free electrons that occur when the beam electron passes through the free electron "gas"[**8**]. The first peak is for only one interaction whereas the number increases to the next plasmon peaks.

The thickness of the sample is then given by[**8**]:

$$t = \lambda \ln \frac{I_l}{I_0} \tag{2.18}$$

Where

t: Thickness of the sample.
λ**:** The mean free path of electrons in the specimen, for Aluminium at 150 kV, $\lambda = 111\ nm$[**21**].
I_l**:** The total intensity in the low-loss spectrum up to 50 eV.
I_0**:** The intensity in the zero-loss peak.

The total intensity is approximated by the intensity in the low-loss spectrum, because the intensity in the spectrum falls rapidly with increasing energy losses this is a reasonable approximation.

2.9.6. HRTEM. The purpose of HRTEM, High-Resolution Transmission Electron Microscopy, is to maximize the useful detail in the image[**8**]. One of the two main problems to get a good HRTEM image is that the lens system is not perfect, some image distortion is unavoidable. The other problem is that we don't know the complete atomic potential and bonding between the atoms through which we must interpret the image.

To get high resolution we need high spatial frequencies[**8**]. Above the sample, the wave function of each electron can be approximated to an incident plane wave. Each electron will interact independently with the specimen. The wave function below the specimen will be a superposition of the incident plane wave and all the diffracted electrons. They will have different phases, and the greatest phase shift is at the atomic columns. The image will be the interference pattern of the electrons with different phases. This is called the phase contrast.

The general specimen transmission function is given by[**8**]:

$$f(x,y) = A(x,y)e^{i\Phi_t(x,y)} \tag{2.19}$$

Where

f(x,y): The specimen transmission function.
A(x,y): The amplitude.
$\Phi_t(x,y)$**:** The phase dependent on the thickness of the specimen.

For simplification, the amplitude is set to $A(x,y) = 1$. The phase change is only dependent on the potential the electron sees going through the specimen and the thickness is assumed to be so small that vi can write a two-dimensional projection of the crystal structure as $V_t(x,y) = \int_0^t V(x,y,z)\,dz$. If the sample is very thin, $V_t(x,y) \ll 1$ and we can approximate the specimen transmission function as[**8**]:

$$f(x,y) = 1 + i\sigma V_t(x,y) \tag{2.20}$$

Where $\sigma = \pi/(\lambda E)$ is called the interaction constant. We have neglected the absorption and the specimen is represented as a "phase object". This is called the weak-phase-object approximation and in general only holds for thin specimens because then the amplitude variations of the wave functions will only slightly affect the image. The amplitude of the transmitted wave function will be linearly related to the projected potential of the specimen[**8**].

The observable contrast in the image is given by the transfer function $T(\mathbf{u})$ by the formula[**8**]:

$$T(\mathbf{u}) = 2A(\mathbf{u})E(\mathbf{u})sin\chi(\mathbf{u}) \tag{2.21}$$

Where

A(u): The aperture function which cuts of all values of **u** greater than a value governed by the aperture radius.

E(u): The envelope function, a property of the lens. Has the same effect as the aperture function.

$\chi(\mathbf{u})$**:** The phase distortion function due to aberrations of the lens and can be written as: $\chi(\mathbf{u}) = \pi\Delta f\lambda u^2 + \frac{1}{2}\pi C_s\lambda^3 u^4$. Δf is the defocus chosen, C_s the lens quality, λ the accelrating voltage and u the spatial frequency.

u: The spatial frequency, $1/x$.

When the transfer function is negative, we have positive phase contrast and the atoms appear dark against a bright background. It is the opposite for a positive transfer function[**8**]. A plot of the transfer function is shown in figure 2.20.

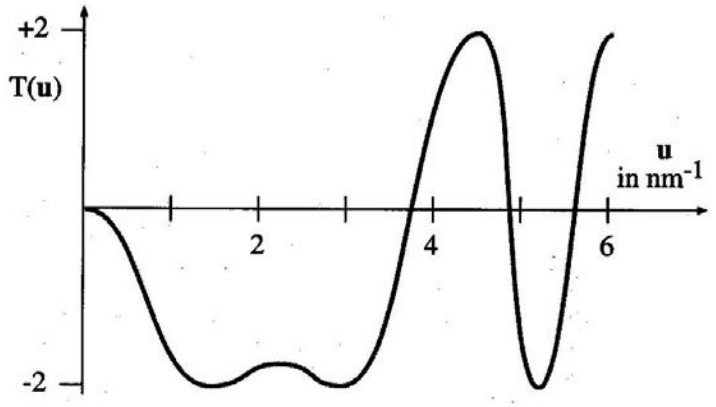

FIGURE 2.20. A plot of $T(\mathbf{u})$ with $C_s = 1\ mm$, $E_0 = 200\ keV$ and $\Delta f = -58\ nm$[**8**].

Because of the zeros in the transfer function, there will be gaps in the output spectrum. The best transfer function will be the function with the lowest number of zeros. In 1949, Scherzer optimized the transfer function by balancing the effect of spherical aberrations

agents a particular defocus value[**8**]. The value, called Scherzer defocus is:

$$\Delta f_{Sch} = -1.2\left(C_s\lambda\right)^{1/2} \tag{2.22}$$

Here, nearly all the beams will have a nearly constant phase until the first zero. This first zero point is called the instrumental resolution limit. This occurs at $u_{Sch} = 1.51C_s^{-1/4}\lambda^{-3/4}$. The resolution is then the reciprocal of u_{Sch} and is $r_{Sch} = 0.66C_s^{1/4}\lambda^{3/4}$. This is the resolution limit where we can use intuitive arguments to interpret what is seen, not the information limit using image processing.

CHAPTER 3

Experimental details

3.1. Alloys

All the alloys investigated were cast at the Research Center at Hydro Sunndal and extruded at SINTEF in Trondheim with the exception of KKAg which was also cast at SINTEF in Trondheim. The alloys were homogenized at 530 ° C for 4 hours before extrusion. They were extruded into long cylinders with a diameter of 20 mm. The alloys were preheated to $540 - 550° C$, then cooled quickly to between $490 - 500° C$ before they were extruded. During the extrusion the temperature increased again, but it was not measured. After the extrusion, the alloys were immediately (within 5 seconds) quenched in cold water.

TABLE 3.1. The alloy compositions in both weight and atomic percentage.

Alloy	**Si**	**Mg**	**Cu**	**Fe**	**Mn**	**Ag**	**Effective Mg/Si-ratio**
KK1 wt%	0.64	0.90	0.40	0.20	0.55	-	2.00
KK1 at%	0.62	1.00	0.17	0.10	0.27	-	
KK2 wt%	0.55	0.90	0.40	0.20	0.08	-	2.00
KK2 at%	0.53	1.00	0.17	0.10	0.04	-	
KK3 wt%	0.90	0.67	0.26	0.21	0.55	-	1.00
KK3 at%	0.87	0.75	0.11	0.10	0.27	-	
KK4 wt%	0.98	0.60	0.51	0.21	0.55	-	0.81
KK4 at%	0.95	0.67	0.22	0.10	0.27	-	
KK11 wt%	0.75	0.81	0.40	0.20	0.55	-	1.50
KK11 at%	0.72	0.91	0.17	0.10	0.27	-	
KK13 wt%	0.52	1.01	0.40	0.20	0.55	-	3.00
KK13 at%	0.50	1.13	0.17	0.10	0.27	-	
KK14 wt%	0.69	0.99	0.45	0.21	0.55	-	2.00
KK14 at%	0.67	1.10	0.19	0.10	0.27	-	
KK15 wt%	0.59	0.81	0.35	0.21	0.55	-	2.00
KK15 at%	0.57	0.90	0.15	0.10	0.27	-	
KKAg wt%	0.64	0.90	0.33	0.20	0.55	0.12	2.00
KKAg at%	0.62	1.00	0.14	0.10	0.27	0.03	

KK1 and KK2 have the same effective Mg/Si-ratio, while both KK3 and KK4 have a surplus of Si. The only difference between KK1 and KK2 is that KK2 have less manganese.

Since manganese prevents recrystallization, it is assumed that KK2 is recrystallized after heat treatment to the T6 condition. T6 is the condition where the alloy is at its peak hardness. KK4 is slightly more Si-rich than KK3, but the main difference here is that the amount of copper is doubled compared to KK3.

KK1, KK2, KK3 and KK4 were mainly part of my project work[**27**], but are included here to compare with the new alloys. KK1 was studied more extensively in this master's thesis.

KK11 was chosen to examine whether a combination slightly lower Mg/Si-ratio than KK1 gave better hardness values, while KK13 was chosen to examine whether a slightly higher Mg/Si-ratio gave a better hardness value. KK14 and KK15 where chosen to examine what hardness changes a slight adjustment of the copper content in the alloy caused. All these alloys were mainly small adjustments to the previous alloys.

The KKAg alloy was chosen because silver has shown to affect the age-hardening of Al-Mg-Si alloys and it stimulates the nucleation of the intermediate precipitates[**28**]. It has also been shown that addition of silver increases the peak hardness of the alloy. An increase in hardness and uniform elongation has also been reported as added benefits of the addition of silver[**17**].

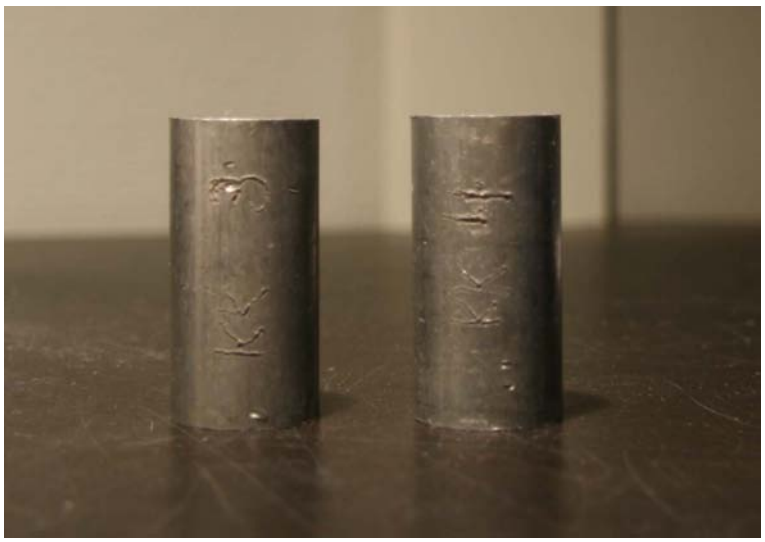

FIGURE 3.1. Two of the cylinders after heat treatment.

These alloys were chosen because it has been shown that copper increases the hardness of aluminium alloys[**11**]. The different choices of Mg/Si-ratios were chosen based on earlier experience of which alloys retains hardness the best[**21**].

12 *cm* were cut of these cylinders and treated to the T6 condition. 5 *cm* of these were then cut of and artificially aged, while the rest were kept in the T6-condition in case something happened to the aged parts, or if it was necessary to investigate the microstructure at an earlier stage than after 100 hours. The stored cylinders in the T6 conditions could then be aged the required time without starting all over again. A picture of some of the heat treated cylinders is given in figure 3.1.

3.2. Heat treatment

Two different heat treatments were performed on the aluminium alloys.

3.2.1. Heat treatment 1. This heat treatment was performed on the KK11, KK13, KK14, KK15 and KKAg-alloys. All five alloys were first treated to SSSS, then aged to achieve the T6 temper of maximum hardness. They were then aged at a high temperature to see what kind of precipitates formed and how long the intermediate phases were present.

The treatment to achieve the T6 temper currently in use[**21**] is as follows:

(1) Solution treatment at 530° C for 30 minutes.
(2) Immediately quenched in water to room temperature.
(3) Storage at room temperature for 4 hours.
(4) Aged at 155° C for 12 hours.
(5) Immediately quenched in water to room temperature.

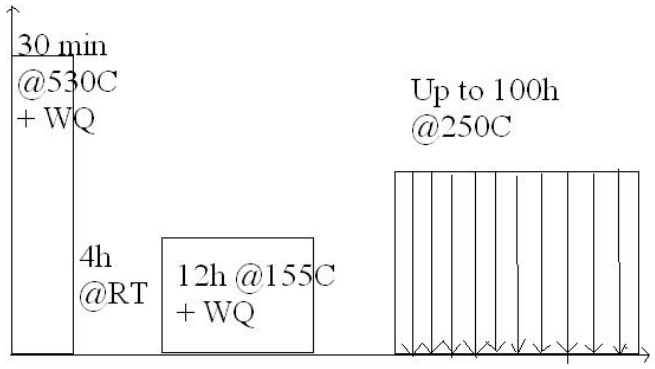

FIGURE 3.2. A schematic overview of heat treatment 1

The solution treatment was carried out in a salt bath, measured to $530 \pm 2°$ C using a digital thermometer. The high temperature created a lot of vacancies which were frozen into the specimen during the subsequent water quench to room temperature. This created the supersaturated solid solution where all the alloying elements are solutes in the aluminium matrix. During the next 4 hours of storage at room temperature, solute

elements and vacancies start to form clusters.

After the 4 hours at room temperature the specimens were put into an oil bath measured to $155 \pm 2°$ C after which the specimens where quickly quenched to room temperature. This was the T6 temper and the specimens were stable and could be kept like this for months. A part of each cylinder was kept in this condition. The complete heat treatment is shown in figure 3.2.

When the specimen were in the T6 condition, the second part of each cylinder were subjected to several heat treatments in a sand bath at 250° C to check the high temperature stability. The same cylinders were heated, water quenched to room temperature and hardness tested before being heated again to a total heat treatment of 100 hours. The hardness was measured after the specimens had a total heat treatment time of 15 minutes, 30 minutes, 1 hour, 1.5 hour, 2 hours, 3 hours, 4 hours, 5 hours, 7 hours, 10 hours, 15 hours, 24 hours, 36 hours, 48 hours, 60 hours, 72 hours and 100 hours.

The temperature variations of the sand bath is given in figure 3.3.

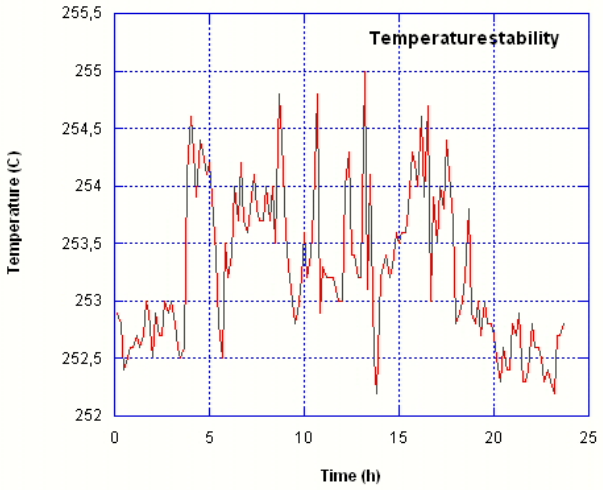

FIGURE 3.3. The temperature variations of the sand bath during 24 hours.

3.2.2. Heat treatment 2. This heat treatment was performed on the KK1, KK13 and KKAg-alloys. They were also first treated to a SSSS, then stored at room temperature and artificially aged at a high temperature to examine what is probably the equilibrium phase. A schematic overview of this heat treatment is shown in figure 3.4

The treatment was:

(1) Solution treatment at 530° C for 30 minutes.
(2) Immediately quenched in water to room temperature.
(3) Storage at room temperature for 4 hours.

(4) Ageing at 350° C for 5 hours.
(5) Immediately quenched in water to room temperature.

The solution treatment and artificial ageing were carried out in the same salt bath used for heat treatment 1(See chapter 3.2.1). The hardness was measured at the end of the heat treatment.

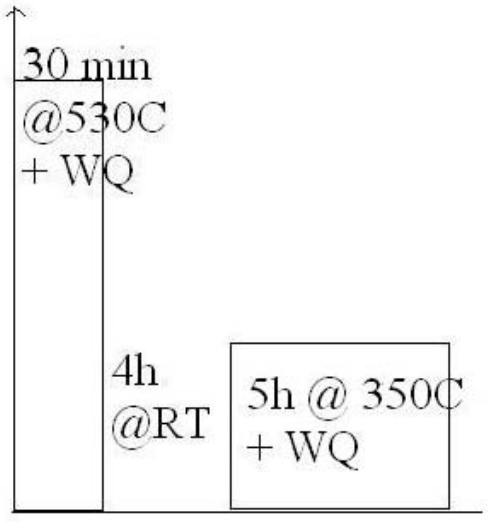

FIGURE 3.4. A schematic overview of heat treatment 2

3.3. Hardness measurement

The measurements of the Vicker Hardness was carried out on an Akashi hardness tester shown in figure 3.5. Five indentations were made on each end of the cylinder after each period of heat treatment. The load used was 5 kg, the pressing time was 15 seconds and the load speed was 100 $\mu m/s$. The corners of the indentations created was then marked on the computer and the computer gave a value for the hardness.

The surface of each cylinder were polished using SiC papers with a fineness up to 1200 grains per cm^2. This made it easier to see the edge of the indentations. Since it was enough room on the end of each cylinder for 10 indentations, the surface was only polished before every second heat treatment.

The ten values measured for the Vickers hardness were then used to calculate a mean value with standard deviations. These are shown in figure 4.1, 4.4 and 4.5.

FIGURE 3.5. The Akashi hardness tester used for measuring the Vickers hardness.

3.4. Specimen preparation

Several small disks were cut from the end of each cylinder using the Struers Accutom 5 shown in figure 3.6(a). They were then grinded down to a thickness of $20 - 100\ \mu m$ using SiC papers of 320, 1200, 2400 and finally 4000 grains per cm^2.

After the grinding, the specimens were cut to the correct size for the TEM using the apparatus shown in figure 3.6(b) and put into small containers where they were kept until they were electropolished.

The electropolishing was done using the Struers Tenupol 3 shown in figure 3.6(c). The electrolyte used was 1/3 nitric acid (HNO_3) mixed with methanol (CH_3OH). The electrolyte was cooled to between $-30°\ C$ to $-20°\ C$. The Ampere meter range was set to 0.5 A, the photo sensitivity to 10, the time to infinite to make sure a hole was etched. The flow rate was set to approximately 6 and the Voltage to 20/60, but both were slightly adjusted between each specimen to keep the current between $0.2 - 0.3\ A$.

A light diode ended the polishing as soon as the specimen had a hole. The specimen were then removed as fast as possible and cleaned in methanol and ethanol to prevent etching, but some of the specimens became etched anyway.

(a)

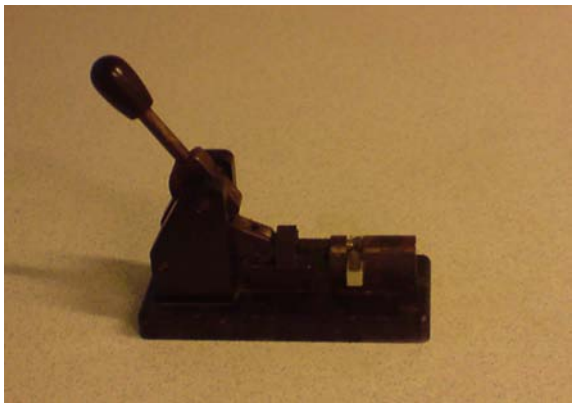

(b)

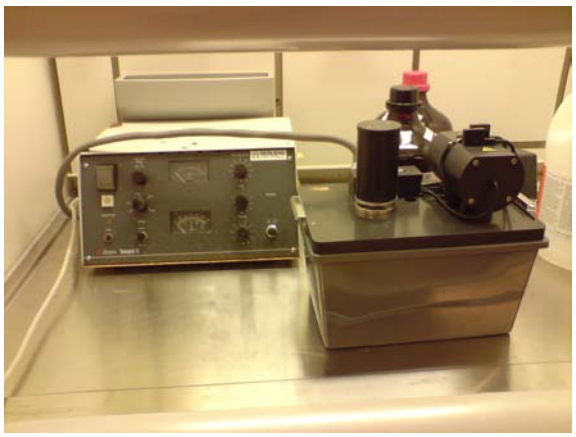

(c)

FIGURE 3.6. (a) The machine used to cut disks of the specimen cylinders., (b) The device used for cutting specimens into the correct size for the TEM sample holder., (c) The machine used for electropolishing.

3.5. TEM

In this master thesis a TEM, Transmission Electron Microscope, was used. It was a Philips CM30 microscope with a tungsten filament and a high voltage of 150 kV. The microscope is shown in figure 3.7. Most of the high resolution images and some of the images used for needle length measurements and number density examinations were taken by Calin D. Marioara.

Two of the high resolution images included from my project work were taken using the JEOL 2010F. Both of these were taken by Calin D. Marioara and this instrument is discussed in more detail in my project work[**27**].

FIGURE 3.7. The CM30 microscope at the Department of physics used for this Master's thesis[**29**].

The specimens were tilted in a ⟨100⟩-direction since that is the direction the precipitates in aluminium grow. A diffraction pattern taken at this zone axis is shown in figure 3.8.

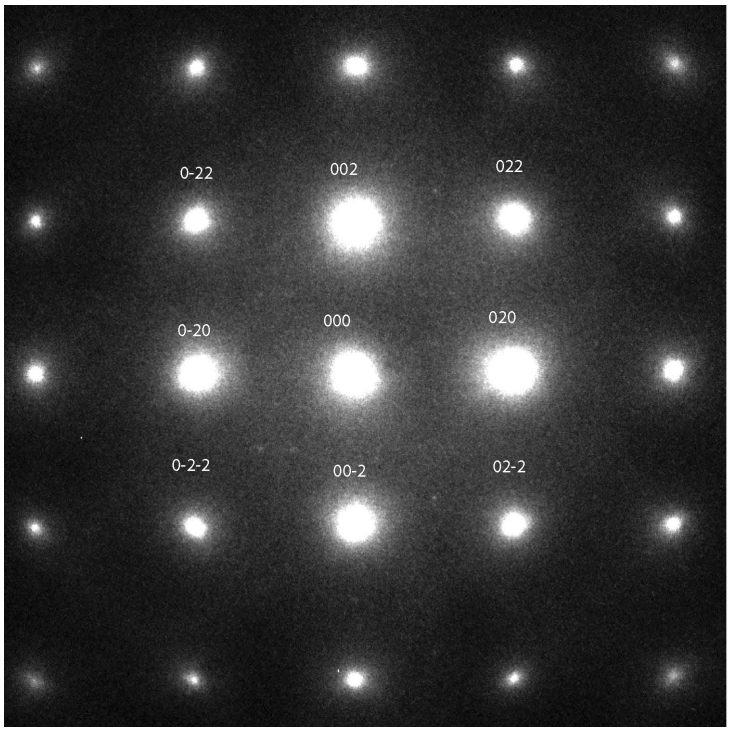

FIGURE 3.8. A diffraction pattern of the ⟨100⟩-direction of Al.

Six pictures of the alloys(KK13 and KKAg) chosen for further studies based on the hardness results after heat treatment 1 were taken at a magnification of $89k$ of each specimen using the CM30. These were used to count the number density and to measure the needle lengths. For both alloys, some pictures were also taken at a magnification of $52k$ in case a lot of the needles were too long to be measured in the pictures used for counting. Six pictures were then taken of both alloys at a magnification of $260k$ to measure the cross-sections of the precipitates. All these pictures are shown in Appendix B. The calculations of the number densities, volume fraction and average cross-sections were carried out using the formulas in section 3.5.1, 3.5.2 and 3.5.3. The high resolution images were taken by using the CCD-camera connected to the CM30 microscope. All the images that have not a comment that they are taken by Calin D. Marioara were taken by the writer of this thesis.

A Gatan (P)EELS was used to measure the thickness of the middle of the area where the pictures were taken. This was only done for the pictures at a magnification of $89k$. To calculate the thickness of the sample, the mean free path of electrons in aluminium must be known. The mean free path is $\tau = 111\ nm$ [**21**].

For the three alloys subjected to heat treatment 2, pictures were taken at a magnification of $10.5k$, $13.5k$ and $17k$. This was mainly to get a qualitative impression of what the microstructure looked like. High resolution images were also taken of these three specimens to examine which phases were present and to try to determine the equilibrium phase.

The XEDS was taken by tilting the specimen 20° toward the detector. This increases the signal received and makes it quicker to collect the XEDS-spectrum. This also increases the signal/noise ratio. The CM30 microscope has a very large copper signal that makes it very difficult to determine the amount of copper present in the specimens. Only the KK1 alloy was examined using XEDS. The precipitates were too small to be able to get any results from the XEDS, but some of the dispersoids were large enough and one of these were analyzed. In addition, one of these dispersoids was checked by indexing of diffraction patterns to find which crystal system it belonged to and to identify the phase.

3.5.1. Needle length. The measured lengths were only from needles in the $\langle 010 \rangle$ and $\langle 001 \rangle$-direction when the images were taken in the [100] zone axis. The specimen was slightly tilted when the images were taken, therefore some of the needles continue through the surface of the specimen. The measured needle lengths will be to short and the average cut needle sticks a distance of $(\langle l \rangle \cos\theta \tan\Phi)/2$ out of the specimen. The length is given by[**30**]:

$$\langle l \rangle = \frac{\langle l \rangle_m}{1 - \frac{\langle l \rangle_m}{t} \cos\theta \tan\Phi} \tag{3.1}$$

Where:

$\langle l \rangle_m$**:** The average measured needle length.

θ**:** The angle showing how [010] and [001] are oriented in respect to specimen geometry[**30**].
Φ**:** The angle the specimen was tilted to obtain a $\langle 100 \rangle$-direction.

3.5.2. Cross-section. The cross-sections of the precipitates were measured on both the images taken at at magnification of $340k$ with the CM30 and the high resolution images taken with the JEOL 2010F. The cross-sections were approximated to either circles (equation 3.2) or rectangles (equation 3.3) to ease the calculation of the sizes[**31**]. They are given below.

$$CS = \frac{\pi d^2}{4M^2} \tag{3.2}$$

$$CS = \frac{ab}{M^2} \tag{3.3}$$

Where:

d: Diameter of the precipitate
a/b: Width/height of the precipitate.
M: The magnification in the picture.

3.5.3. Number density and Volume fraction. Some of the needles in the $\langle 100 \rangle$-direction that was counted in the images are also not entirely in the specimen, i.e. they are cut. The number of precipitates counted are therefore from a larger volume than calculated using the thickness from the (P)EELS and the area of the picture taken. Each cut needle has an average of $\langle l \rangle /2$ outside the measured volume. In addition, only the needles along the $\langle 100 \rangle$-direction is counted in these alloys because the number density is quite high. The volume corrected number density is then[**30**]:

$$\rho = \frac{3N}{At(1 + \frac{\langle l \rangle}{t})} \tag{3.4}$$

Where:

N: Counted number of needles in the $\langle 100 \rangle$-direction.
A: The real area of which the needles are counted, i.e. $A = A'/M^2$.
t: The thickness of the specimen measured using (P)EELS.
$\langle l \rangle$**:** The average length of the needles.

The volume fraction(VF) is given by[**30**]:

$$VF = \langle CS \rangle \langle l \rangle_m \langle \rho \rangle \tag{3.5}$$

This volume fraction should be close to the amount of alloying elements present in the alloy given that all the solute elements are in precipitates.

3.6. Image treatment

The negatives were developed using the Kodak D-19 Developer. They were kept in the developer for five minutes with periodic shaking of the image holder. They were then rinsed for three minutes in running water before they were put in the Kodak fixer for six minutes. After this, the negatives were rinsed in running water for more than half an hour.

The negatives were scanned using an Epson Perfection 4990 Photo scanner at 600 dpi, 16-bit grayscale. The document type selected was Film(with Film Area Guide) and the Film Type was B&W Negative Film.

Most of the high-resolution images were enhanced using Gatan DigitalMicrograph. The image before enhancement is shown in figure 3.9(a). The image after enhancement is shown in figure 3.9(d). The first image is transformed into figure 3.9(b) using a Fast Fourier Transform(FFT)-algorithm in the program. A function called BandpassMask is then chosen and all spatial frequencies below 0.5 nm is removed. The BandpassMask only lets the part of figure 3.9(b) shown in figure 3.9(c) through. An inverse FFT is then performed and the result is as shown in figure 3.9(d). One of the problems with this method is that information is removed and artifacts may be embedded in the images.

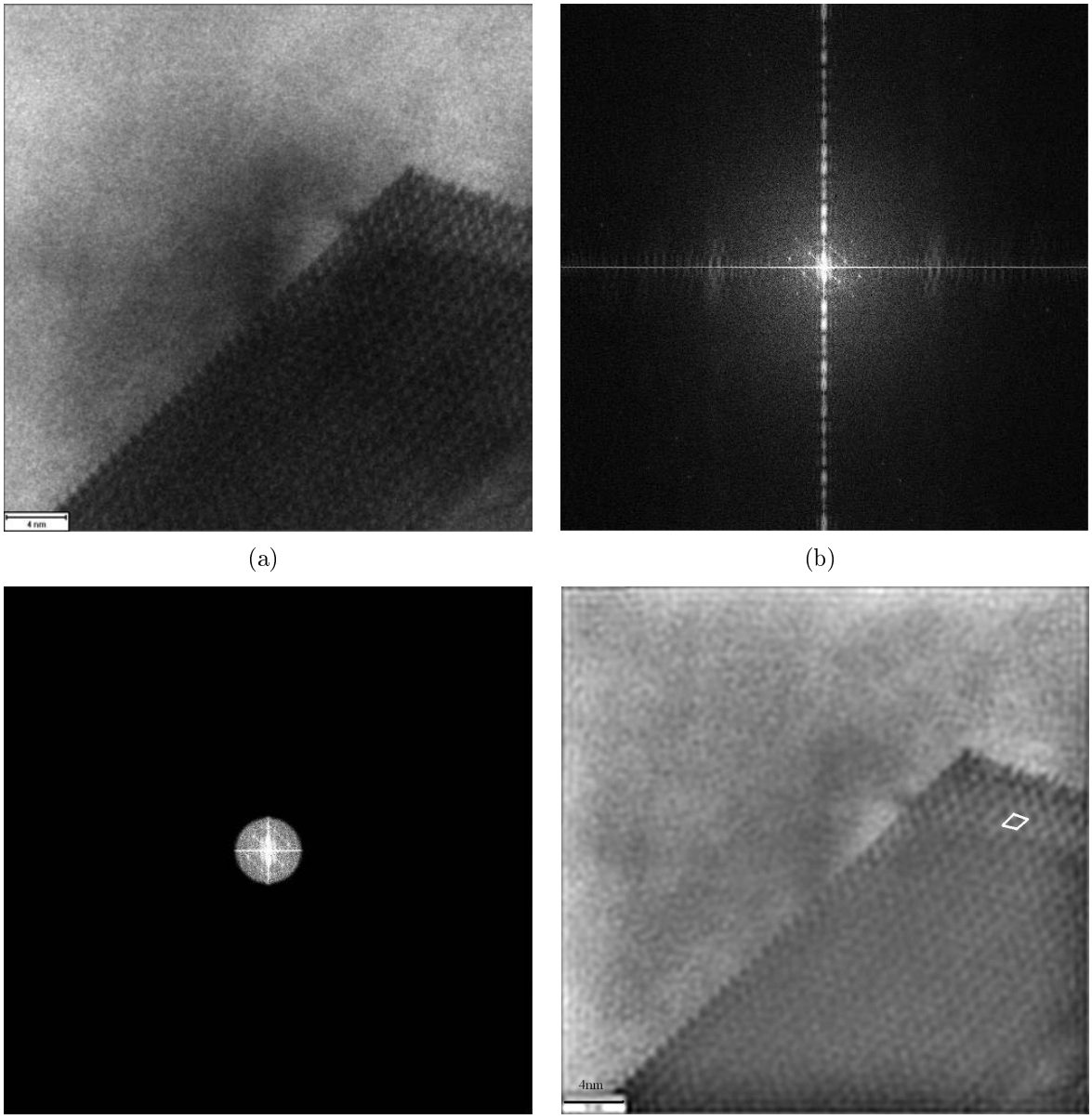

(a) (b)

(c) (d)

FIGURE 3.9. (a) and (d) shows the same image before and after image treatment. (b) shows the FFT of (a) while (c) shows the filtering mask used to enhance the image.

CHAPTER 4

Results and discussion

4.1. Summary of project work

Since this work is a continuation of my project work, a brief summary is given here. For a complete discussion and results, see [**27**].

The hardness results are shown in figure 4.1. These alloys were all exposed to heat treatment 1.

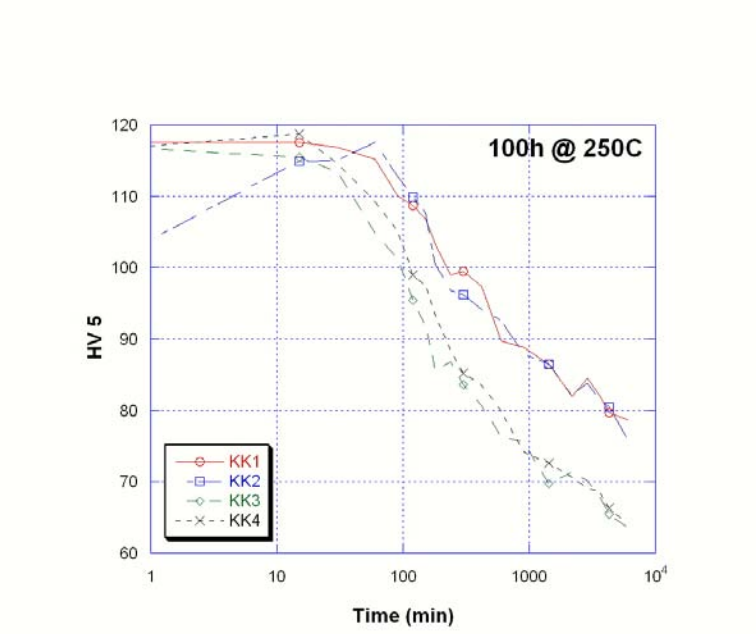

FIGURE 4.1. Graph of the results from hardness measurements.

As can be seen in figure 4.1, the hardness of KK1 and KK2 follow each other closely after the first 30 minutes. The hardness of KK3 and KK4 declines faster and earlier than that of KK1 and KK2. KK1 and KK4 were chosen for number density and precipitate studies.

Figure 4.2 clearly shows that the microstructure of the KK4 alloy is much coarser and less dense than the microstructure of the KK1 alloy. This is clearly shown in table 4.1

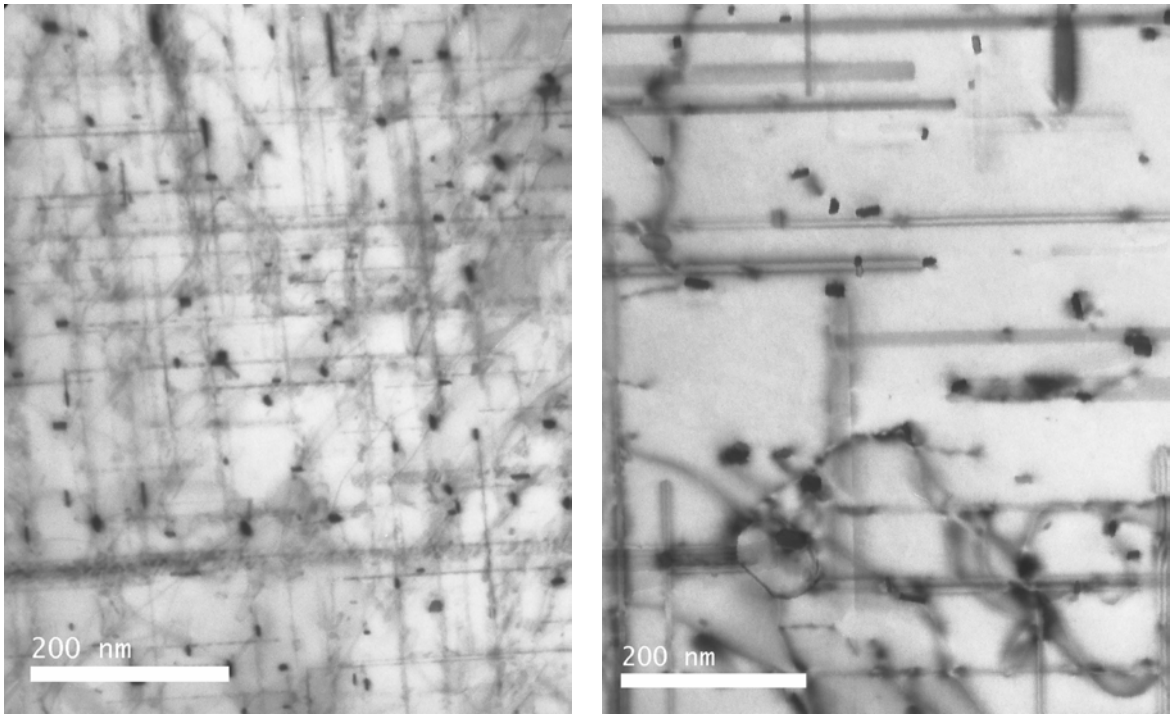

(a) (b)

FIGURE 4.2. (a) An image showing the microstructure of the KK1 alloy, (b) An image showing the microstructure of the KK4 alloy. Both images were taken by Calin D. Marioara.

where the results of the measurements are shown. Clearly the volume fraction of the KK4 is overestimated due to the very long needles in this alloy.

TABLE 4.1. The volume fraction, number density, average needle length and cross-sections of the investigated alloys.

Alloy	**Volume fraction** (%)	**Number density** (μm^{-3})	**Needle length** (nm)	**Cross section** (nm^2)	**Solute content (Mg+Si)** (%)
KK1	1.81 ± 0.237	1183 ± 134	235.2 ± 7.4	65.2 ± 8.30	1.62
KK4	3.07 ± 0.428	418 ± 51.3	437.6 ± 16.4	211.5 ± 28.41	1.62

High resolution images of these two alloys are shown in figure 4.3.

The high resolution images shown in figure 4.3 show that the KK1 alloy have both platelike (probably C-phase) and Q'-precipitates. Figure 4.2(a) shows that most of the long axis of the cross-sections of the precipitates, mostly platelike, in the KK1 alloy are aligned along the needles, in the ⟨100⟩-direction, but with some Q'-precipitates along the ⟨510⟩-direction. In the KK4 alloy, most of the precipitates are Q', aligned along the ⟨510⟩-direction. This can be clearly seen in figure 4.2(b). A phase transformation into

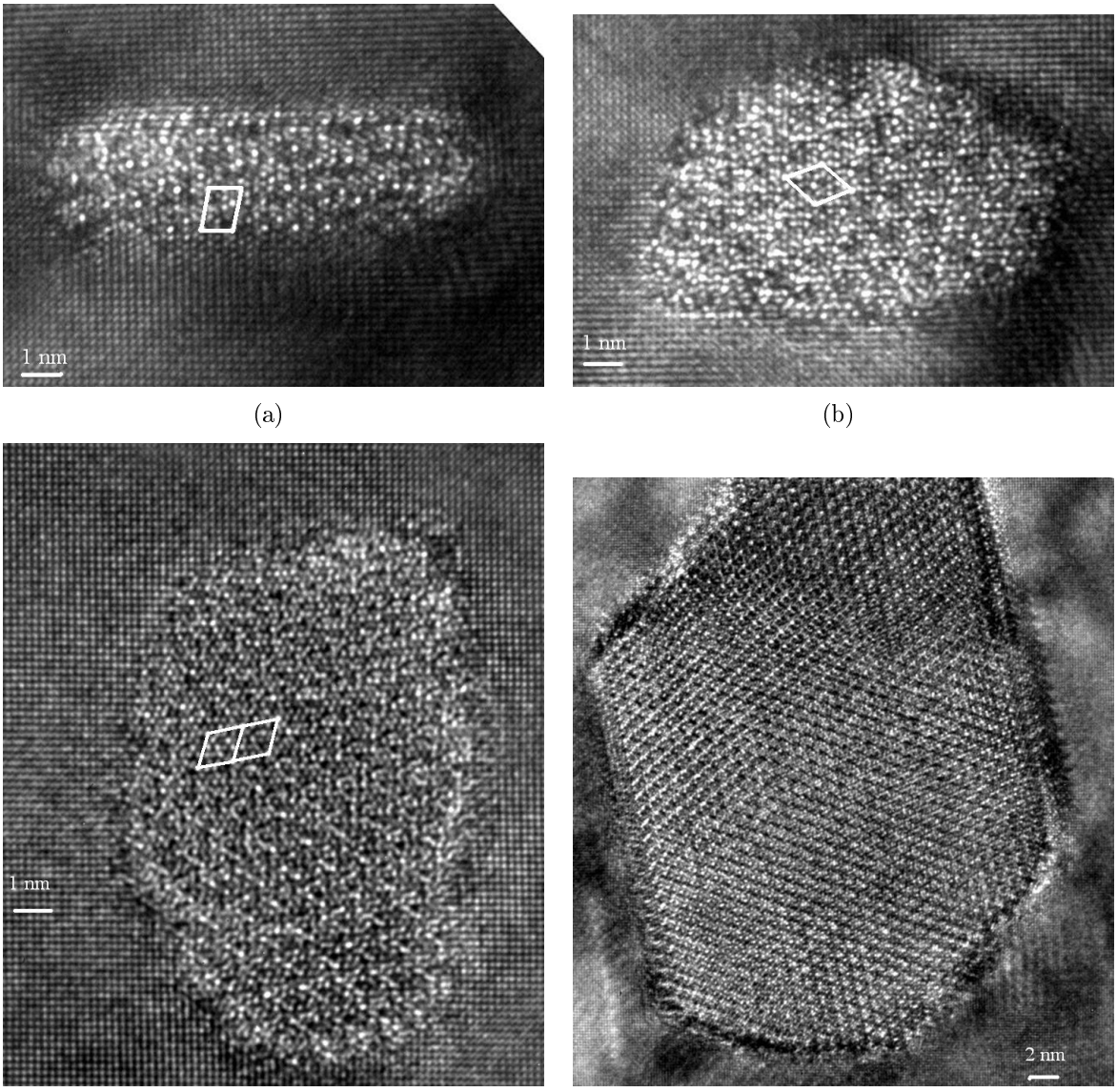

FIGURE 4.3. (a) Platelike precipitate in the KK1 alloy, (b) Q'-precipitate in the KK1 alloy, (c) Q'-precipitate in the KK4 alloy, (d) Large Q'-precipitate in the KK4 alloy. All these images were taken by Calin D. Marioara.

Q' has barely begun in the KK1 alloy while in the KK4 most of the precipitates are Q'. The difference in number density and coarseness of the particles is the main reason for the differences in hardness between the two alloys.

4.2. Hardness measurements

4.2.1. Heat treatment 1. The hardness results of the alloys are shown in figure 4.4 and figure 4.5. The measured values are shown in table A.1.

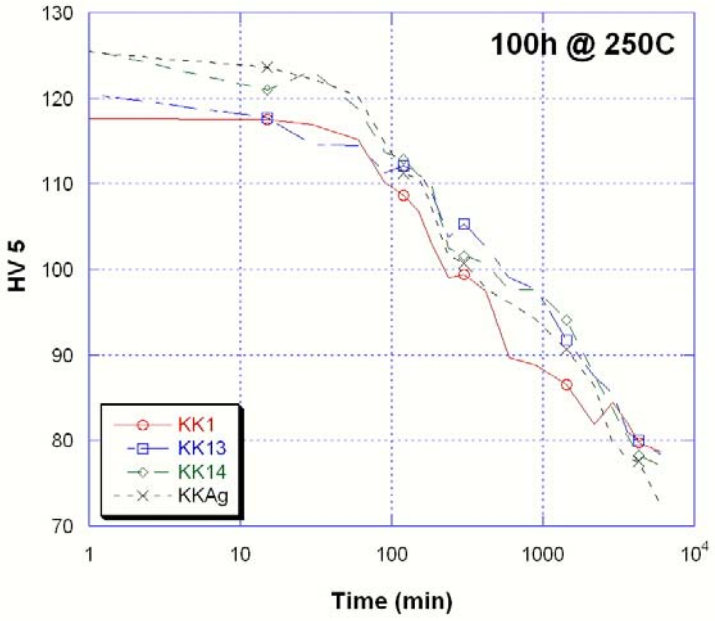

FIGURE 4.4. Hardness results of the three alloys with the highest hardness. KK1 from the project work is also included to make it easier to compare.

At the start of the heat treatment, KK14 and KKAg have the highest hardness with 125.7 and 125.5 respectively. This supports earlier research[**17**], that the addition of silver increases the peak hardness. The KKAg alloy does this compared to the same alloy without silver, the KK1 alloy. The peak hardness of the KK1 alloy is 117.6. At this point, KK11, KK13 and KK15 have a hardness of about 120. After 100 hours of heat treatment, the KK13 alloy has the highest hardness with a value of 78.4. KK14 is close behind with a hardness of 77.1. KKAg has a hardness of 72.4, KK11 has 65.9 and KK15 has 69.5.

All the alloys more or less retain their hardness for the first 90 minutes. After this period, they start to lose hardness at a varying speed. KK13 is the alloy which retains the hardness the best. As can be seen in figure 4.4, after two hours of heat treatment, the KK13 alloy has the highest hardness and it mostly retains the highest hardness until the end of the heat treatment after 100 hours. The hardness is mostly just barely better than that of the KK14 alloy. After 48 hours and onwards, KK1 and KK13 have approximately

the same hardness and are slightly better than KK14.

KKAg clearly has a lower hardness after 100 hours of heat treatment than the three other alloys. It drops sharply between 36 and 48 hours. After 36 hours of heat treatment, KKAg has approximately the same hardness as KK13 and KK14. At the next measurements, after 48 hours of heat treatment, the hardness is almost 5 points below that of the other alloys.

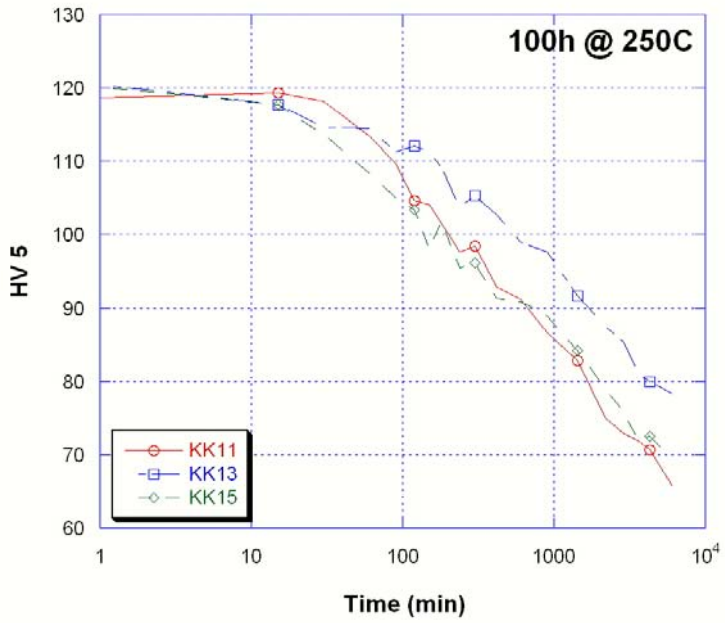

FIGURE 4.5. Hardness results of the two alloys with the lowest hardness. KK13 is included to make it easier to compare.

Figure 4.5 shows, that both KK11 and KK15 start out at approximately the same hardness as KK13. KK11 follows KK13 for the first hour while KK15 only follows the KK13 alloy for the first half hour. After this period of time, both these alloys decline faster than the KK13 alloy, but KK11 declines faster than KK15. KK11 has a higher hardness than KK15 from 15 minutes until 10 hours of heat treatment. The hardness of the KK15 alloy declines fast for the first 2.5 hours, after this the hardness of the KK11 alloy declines faster and passes the hardness of KK15. After 36 hours, both alloys decline at approximately the same speed.

TEM-samples were chosen from KK13 and KKAg. KK13 was chosen because this was the alloy that retained its hardness the best during the heat treatment. KKAg was chosen

to investigate what effect the addition of a small amount of silver has on the microstructure of the alloy. It was assumed that the microstructure of the KK14 alloy was the same as that of the KK1 alloy shown in figure 4.2(a), because the only difference between these two alloys are slightly less copper in the KK14 alloy than in the KK1 alloy. KK11 and KK15 were not chosen for further studies due to their lower hardness values.

The TEM specimens were measured for cross-sections, number densities and needle lengths.

4.2.2. Heat treatment 2. The hardness values of the alloys after heat treatment 2 are shown in table 4.2.

TABLE 4.2. The hardness measured after 5 hours at 350° C

	KK1	**KK13**	**KKAg**
HV 5	49.8 ± 0.66	49.6 ± 0.31	50.5 ± 0.22

After this heat treatment, all the hardness values converge. The convergence of the hardness values indicates that all the alloys probably end in the same phase. All these alloys were chosen for investigation using TEM to confirm whether the alloys contain the same phases or not. The alloys were also checked qualitatively as to whether the microstructure of the different alloys was comparable. One of the dispersoid phases were also investigated using EDX and diffraction patterns.

4.3. Microstructure after heat treatment 1

Both KK13 and KKAg were investigated using bright field TEM-images. All the images used for number density counting, length measurements and cross-section measurements are shown in appendix B.

The calculated values are shown in table 4.3. The images of KK13 are shown in figure 4.6, while the images of KKAg are shown in figure 4.7.

TABLE 4.3. The volume fraction, number density, average needle length and cross-sections of the investigated alloys.

Alloy	**Volume fraction** (%)	**Number density** (μm^{-3})	**Needle length** (nm)	**Cross section** (nm^2)	**Solute content (Mg+Si)** %
KK13	0.87 ± 0.12	1181 ± 102	240.2 ± 7.24	30.8 ± 1.5	1.65
KKAg	1.36 ± 0.17	477 ± 45	410.3 ± 15.3	69.5 ± 6.9	1.62

By comparing figure 4.6(a) and 4.6(b) with figure 4.2(a) it can be seen that the density of the precipitates are approximately equal. The average needle length of these alloys are

measured to nearly equal. The cross-sections of the KK13 alloy is measured to be less than half of that of the KK1 alloy. The reason for this could be that for the KK13 alloy, all cross-sections were measured on pictures taken with a magnification of $260k$, while for the KK1 alloy, some of the cross-sections were measured at a magnification of $89k$, making it harder to measure the really small precipitates. The difference in cross-sections also explains the differences in the volume fraction.

It looks like more of the precipitates in the KK13 alloy have the long edge of the cross-section aligned along the $\langle 100 \rangle$-direction of aluminium. Most of these precipitates look to have a very thin and long cross-section, mainly looking platelike. For the KK1 alloy, some transformation into Q'-precipitates aligned along the $\langle 510 \rangle$-direction was observed[**27**].

The comparable numbers and sizes of the precipitates in the KK1 and KK13 alloy explain the convergence of the hardness of these two alloys. As shown in section 2.6, the strength of the alloy is closely connected to the density of the precipitates and their sizes.

Comparing figure 4.6 and figure 4.7, it can clearly be seen what the numbers in table 4.3 shows. The needle lengths in the KKAg alloy are longer than in KK13, the cross-sections are larger and the number density is much lower. The coarser precipitates explains the lower hardness of the KKAg alloy compared to both KK1 and KK13 as explained in section 2.6.

In figure 4.7 it can also be seen that a lot of the precipitates are oriented along the $\langle 510 \rangle$-direction. A transformation from the platelike precipitates along the $\langle 100 \rangle$-direction has occured. This transformation has barely started in the KK13 alloy in figure 4.6.

Mostly, the numbers, with the exception of cross-section size, of KKAg are close to those of KK4 shown in table 4.1. The needle lengths of KK4 were underestimated because most of the really long needles didn't end within the images, making it impossible to measure their length. This was also the case for the images taken at $89k$ of the KKAg alloy, but now some pictures were also taken at $52k$ to make sure that the needle length was measured more accurately.

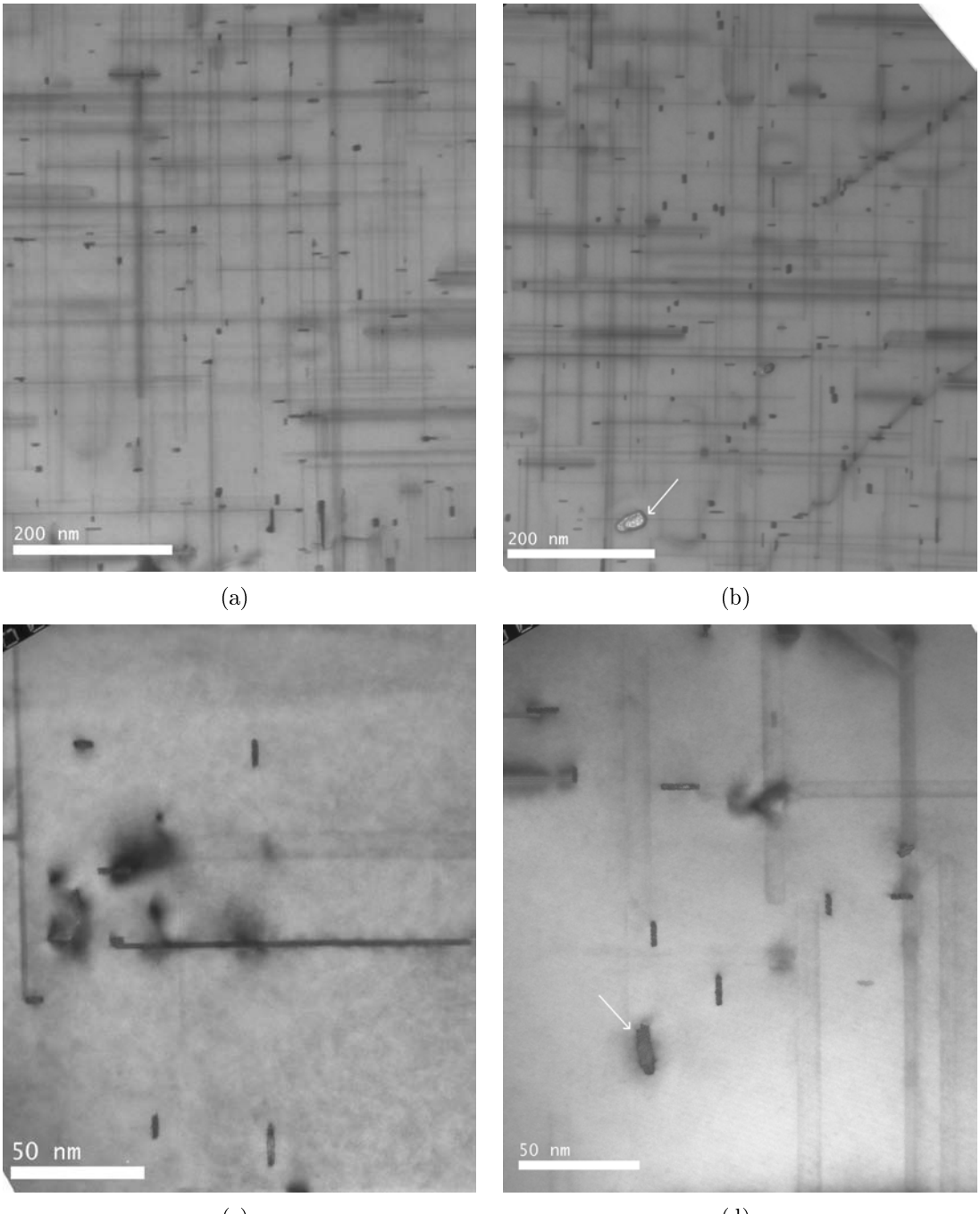

(a) (b)

(c) (d)

FIGURE 4.6. (a) and (b) Bright field images of the KK13 alloy. An etched precipitate can be observed in (b) (Arrow). (c) and (d) High-resolution bright field images of the KK13 alloy. A precipitate oriented along the ⟨510⟩-direction can be seen (Arrow). All these images were taken by Calin D. Marioara

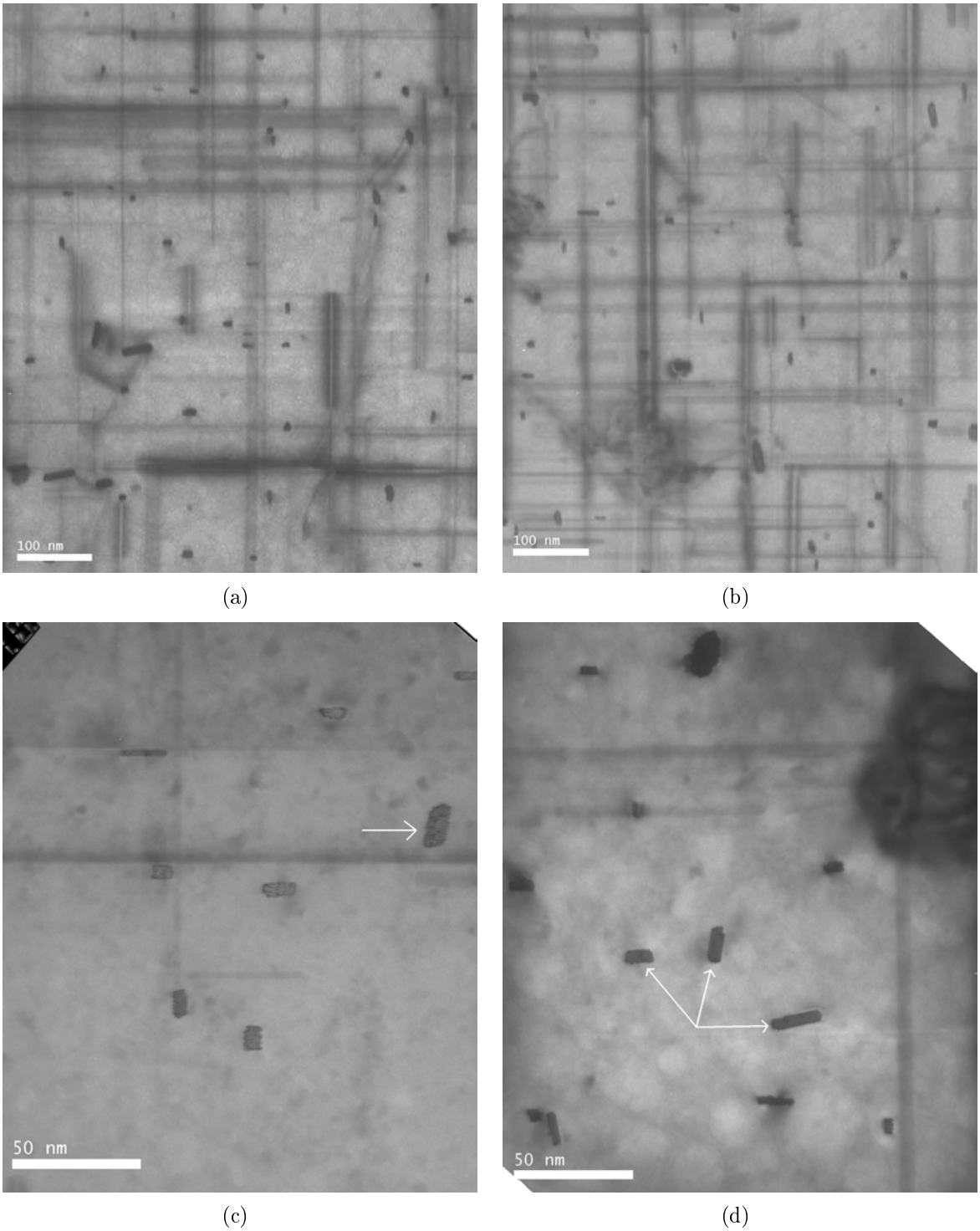

(a) (b)

(c) (d)

FIGURE 4.7. (a) and (b) Bright field images of the KKAg alloy. (c) and (d) High-resolution bright field images of the KKAg alloy. Here you can see an oxide layer on the surface of the specimen. Also, some precipitates oriented along the ⟨510⟩-direction can be seen (Arrows). All these images were taken by Calin D. Marioara.

4.4. Microstructure after heat treatment 2

The microstructure of the KK1, KK13 and KKAg alloys looks similar after heat treatment 2. This can be seen by comparing figures 4.8(a), 4.9(a) and 4.10(a). These images are tilted slightly out of the ⟨100⟩-direction so that the dislocation network is not visible. The density of the precipitates and dispersoids looks to be about the same, the lengths and cross-sections of the needles looks similar. In all these pictures, it can clearly be seen that a lot of the precipitates nucleate on the dispersoids. Nucleation on an existing interface requires lower energy than nucleation in the matrix[**2**]. It is however only for the KK1 and KK13 alloy that some of the precipitates still have cross-sections oriented along the ⟨100⟩-direction. This indicates that a small amount of a different precipitate-type is present in these two alloys.

Figure 4.8(b) shows a low-angle grain boundary where the grain in the upper right corner is aligned closer to the zone-axis. At this grain boundary, a higher number of precipitates and dispersoids can be observed. Figure 4.8(c) and 4.8(d) shows the large dislocation network in this specimen. In figure 4.8(d), there is also a large particle in the lower part of the picture. The composition of this particle has not been investigated. In figure 4.8(a), it can be seen that a lot of the needles are lying along another direction than the ⟨100⟩-direction. This is due to the needles sticking out of the specimen and falling along the surface. It is because of the long needles this is so visible.

Both in figure 4.9(a) and 4.9(b), bright field images of the KK13 alloy, a grain boundary can be seen. In both cases, a high number of precipitates and dispersoids have nucleated on this grain boundary. Also with this specimen, needles lying along the surface of the specimen can be observed. Figure 4.9(c) shows how the precipitates nucleate of the dispersoids at a higher magnification. The dislocation network is shown in figure 4.9(d). Here it can also clearly be seen that the precipitates nucleate at dispersoids.

Figure 4.10(a) of the KKAg alloy shows that the precipitates of this alloy also often precipitate on the dispersoids. It is also visible that some needles are lying along the surface of the specimen, not along the ⟨100⟩-direction. By looking at figure 4.10(b), it can be seen that the precipitates also nucleates on grain boundaries. There is also a high number of dispersoids on these low angle grain boundaries. In this figure, two triple points can also be seen. This is the most energetically favorable meeting point of grains[**2**].

The dislocation network of the KKAg alloy is clearly visible in the upper right corner of figure 4.10(c). In this figure, a grain boundary with some precipitation is also visible. Figure 4.10(d) shows the same area at a lower magnification. In this figure it is visible how the needles sticking out of the surface are lying along the surface and not along the ⟨100⟩-direction.

A high number of the precipitates in all these alloys nucleate either at the grain boundary or on dispersoids. The nucleation is clearly heterogeneous.

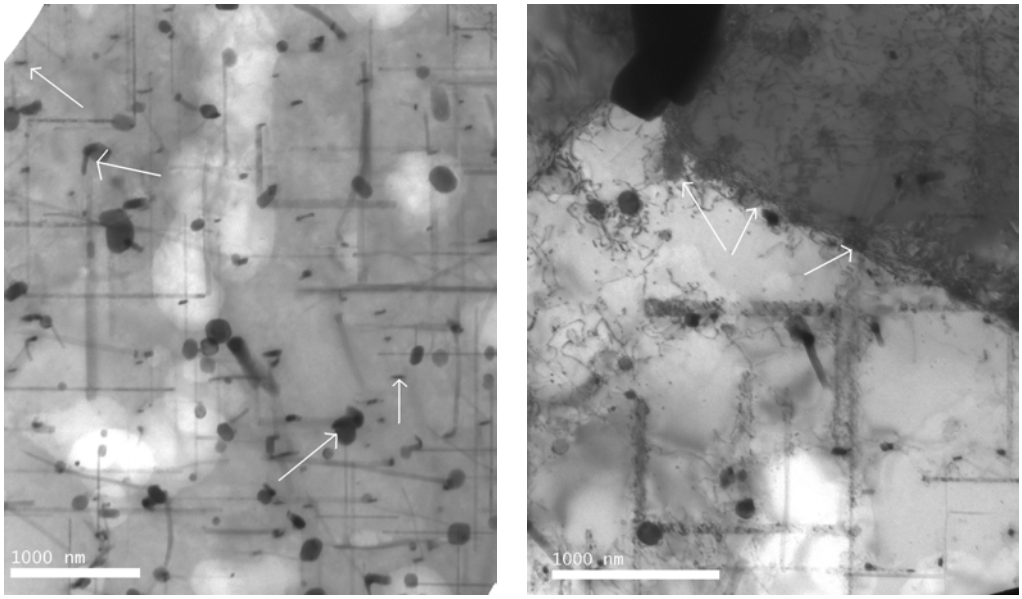

(a) (b)

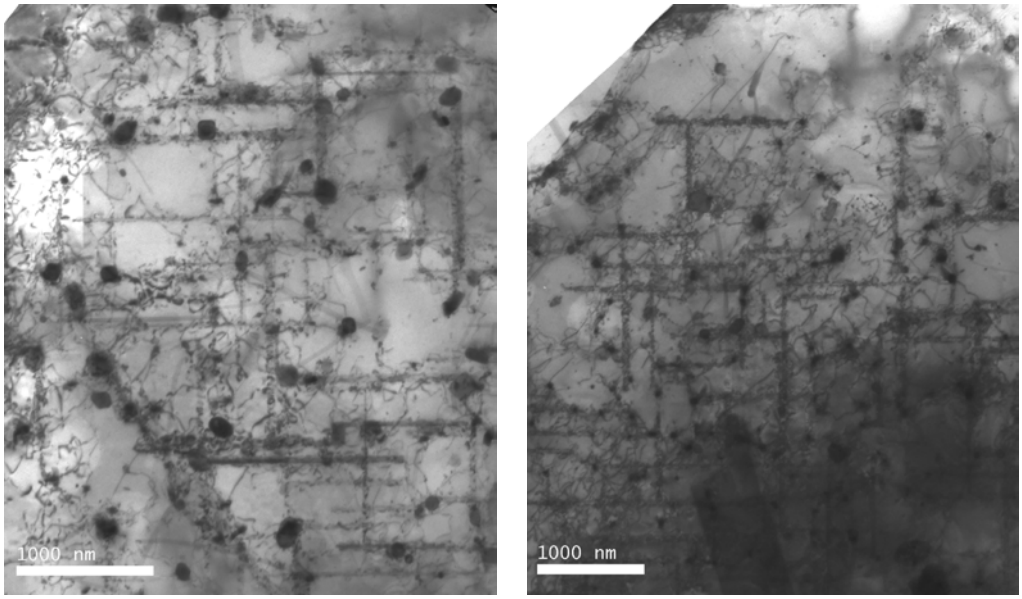

(c) (d)

FIGURE 4.8. (a) Bright field image of the KK1 alloy. Notice all the cut needles lying along the surface of the specimen. Also notice the high number of precipitates nucleating on the dispersoids (Arrows). Also, a few of the precipitates are oriented along the ⟨100⟩-direction (Arrows). (b) Bright field images of the KK1 alloy. Notice the high number of precipitates and dispersoids nucleated on the grain boundary (Arrows). (c) and (d) Bright field images of the KK1 alloy. Notice the large dislocation network. It is still possible to see a high number of precipitates nucleated on the dispersoids.

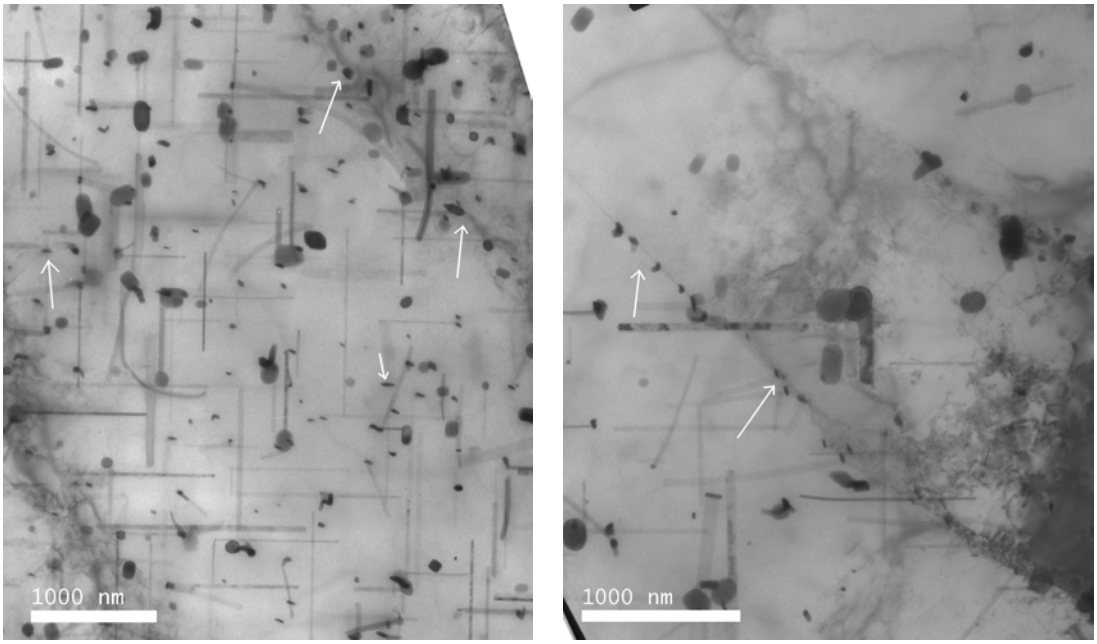

(a) (b)

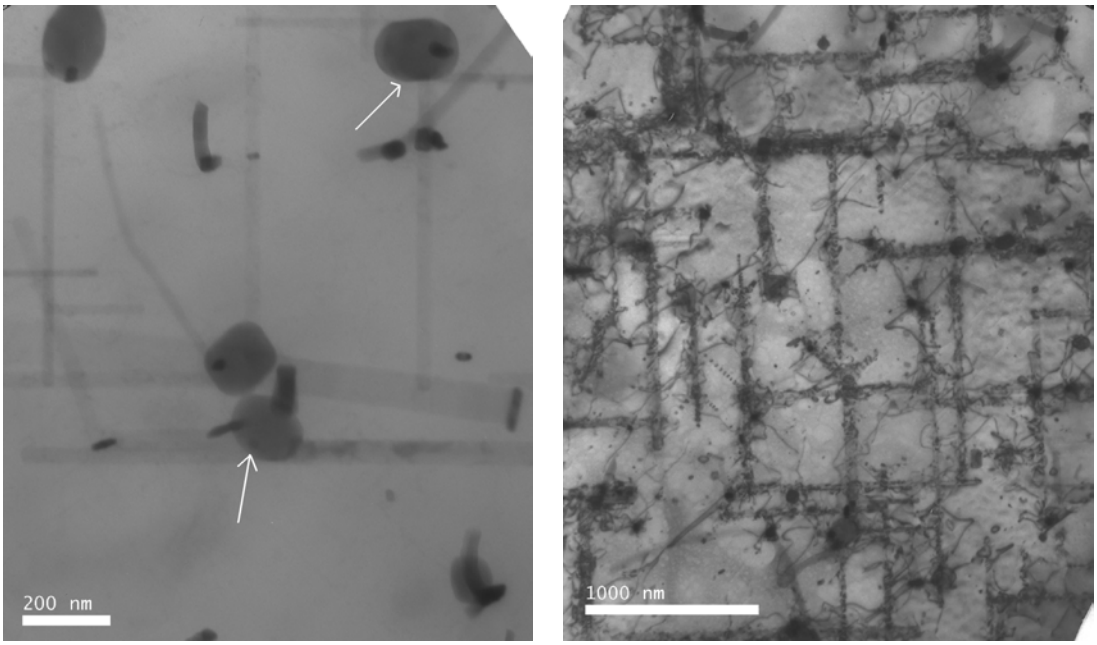

(c) (d)

FIGURE 4.9. (a) and (b) Bright field images of the KK13 alloy. Notice how the precipitates nucleate on the dispersoids and on the grain boundaries (Arrows). A few of the precipitates are oriented along the ⟨100⟩-direction (Arrows). (c) Bright field image of KK13 which gives a better view of how the precipitates nucleate of the dispersoids (Arrows). (d) Bright field image of the KK13 alloy showing the large dislocation network. Some nucleation on dispersoids is visible in this image as well.

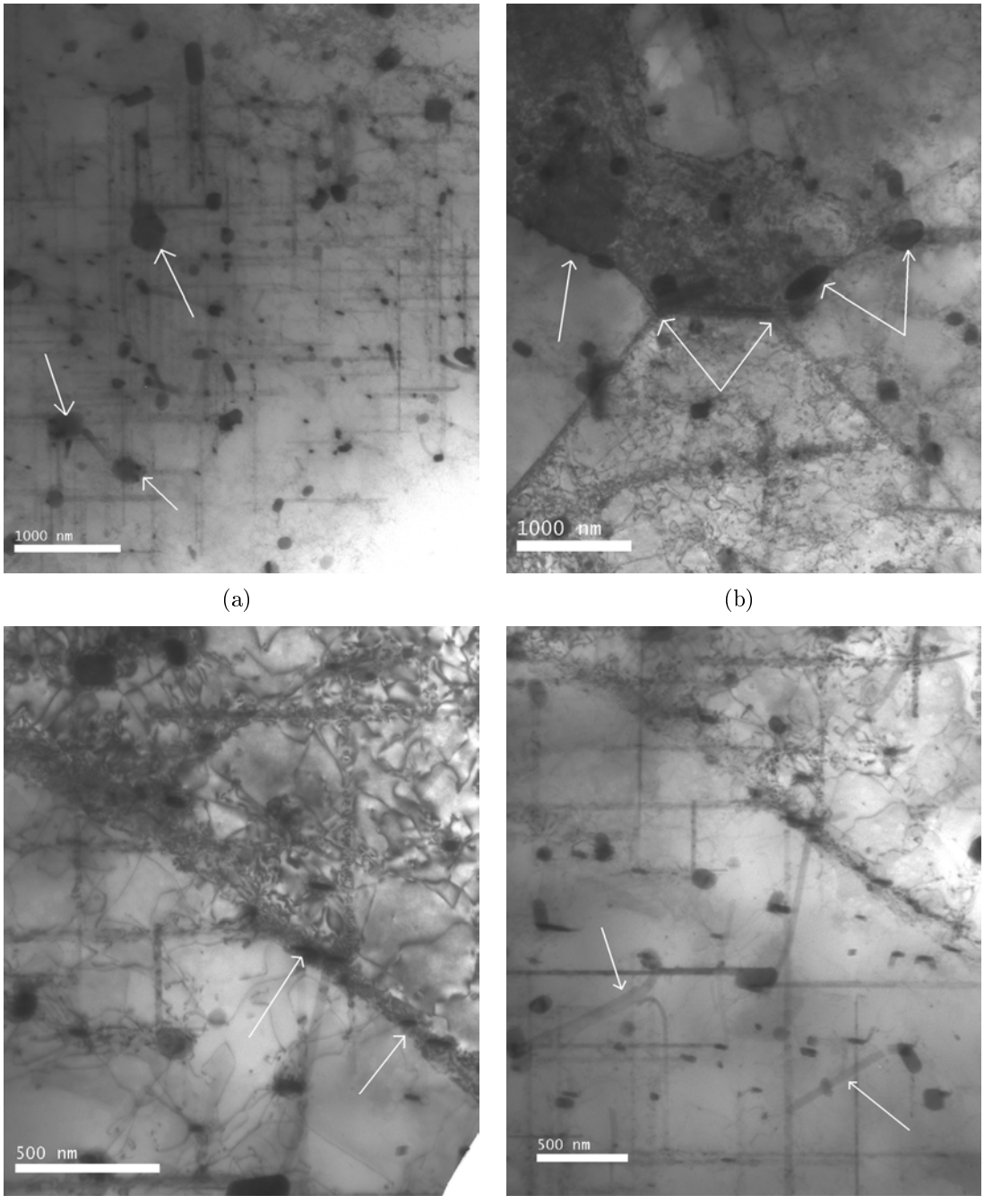

(a) (b)

(c) (d)

FIGURE 4.10. (a) Bright field image of the KKAg alloy. Notice how the precipitates nucleate on the dispersoids (Arrows). (b) Bright field images of the KKAg alloy. Notice the two triple points and the nucleation along the grain boundaries (Arrows). (c) and (d) Bright field images of the same area. Notice the dislocation network and how some parts of the needles are lying along the surface (Arrows). It is also possible to see how the precipitates nucleate on the grain boundary (Arrows).

4.5. HRTEM

4.5.1. KK13 after heat treatment 1. Figure 4.11 shows high-resolution images of the KK13 alloy. In figure 4.11(a) a precipitate clearly oriented along the ⟨100⟩-direction is shown. The needles are included to confirm that the precipitate is oriented along this direction. This is a platelike precipitate.

Figure 4.11(b) shows a precipitate with a long and thin cross-section. A lot of the precipitates were similar to this and even though little structure can be seen in this image, it is probably a disordered platelike precipitate. These kinds of precipitates looked to be more common in the KK13 alloy than in the KK1 alloy studied in my project work[**27**].

The Q'-precipitate in figure 4.11(c) is included to show that some transformation into the Q'-phase has happened. In this image the hexagonal unit cell with a periodicity of approximately 1 nm can be seen. This also happened in the KK1 alloy, some transformation from the platelike to the Q'-precipitate has started, but most of the precipitates have not been transformed yet.

In figure 4.11(d) the precipitate is still oriented along the ⟨100⟩-direction. The unit cell of this precipitate has a periodicity of 0.7 nm which might mean that this precipitate is a S-precipitate as explained in table 2.2.

In the KK13 alloy, several different types of precipitate have been found. Some precipitates with some transformation into the Q'-phase with the rest of the precipitate disordered was found. This probably means that a transformation into the Q'-phase has started to happen, but is yet to finish. This is just as it was in the KK1 alloy[**27**].

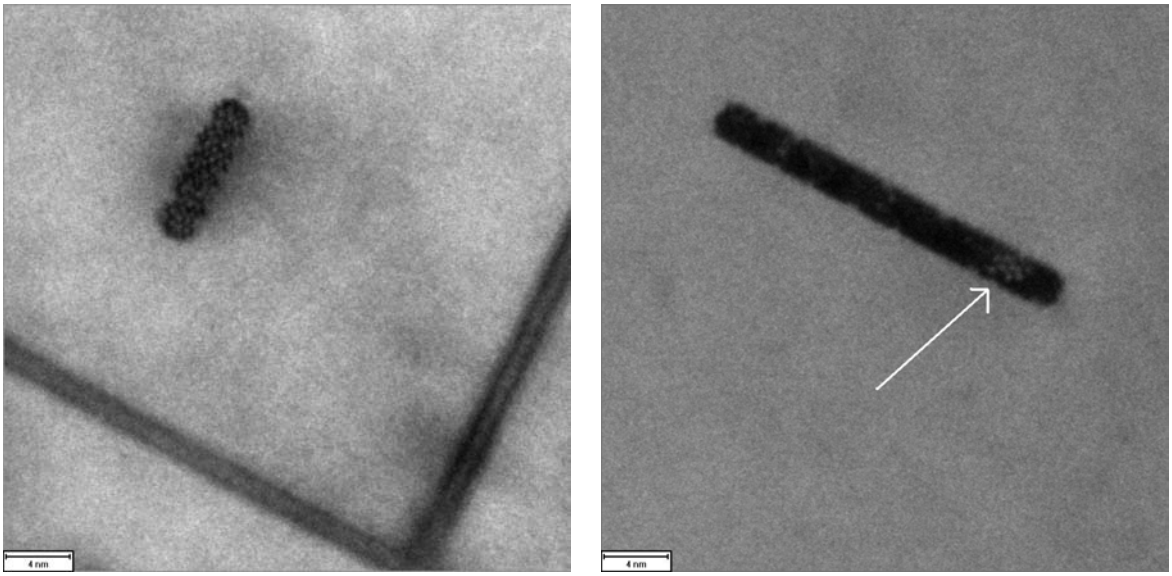

(a) (b)

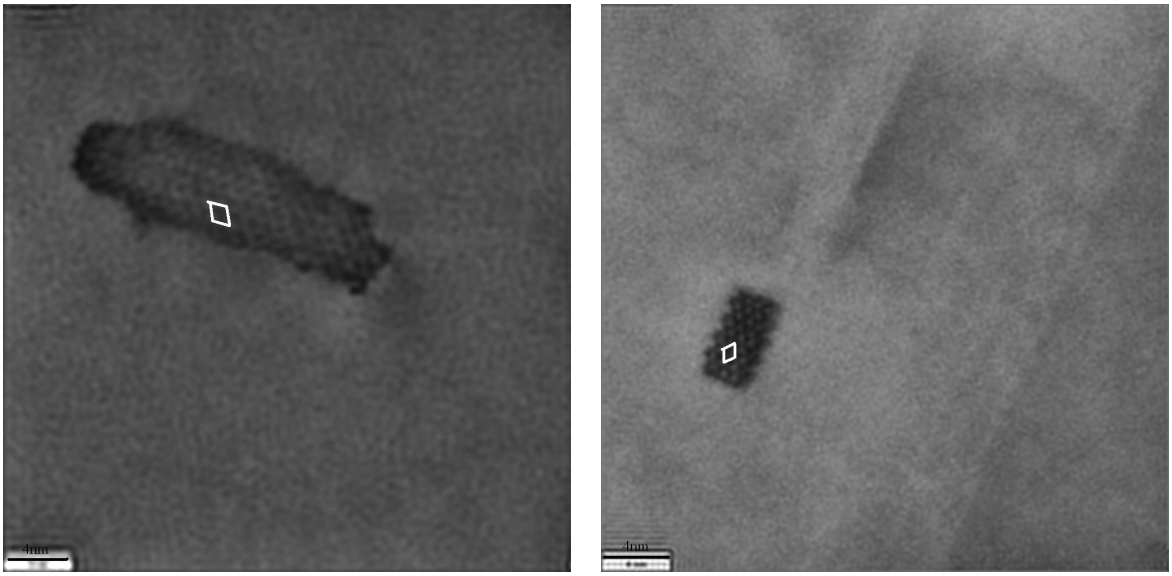

(c) (d)

FIGURE 4.11. All these images are taken of the KK13 alloy by Calin D. Marioara. (a) This image shows a disordered platelike precipitate oriented along the ⟨100⟩. (b) A narrow and long platelike precipitate with some visible ordering (Arrow). (c) A Q'-precipitate with a unit cell superimposed. (d) A short and thick platelike precipitate, probably S-type with a unit cell superimposed. Both (c) and (d) are Fourier-filtered as explained in chapter 3.6

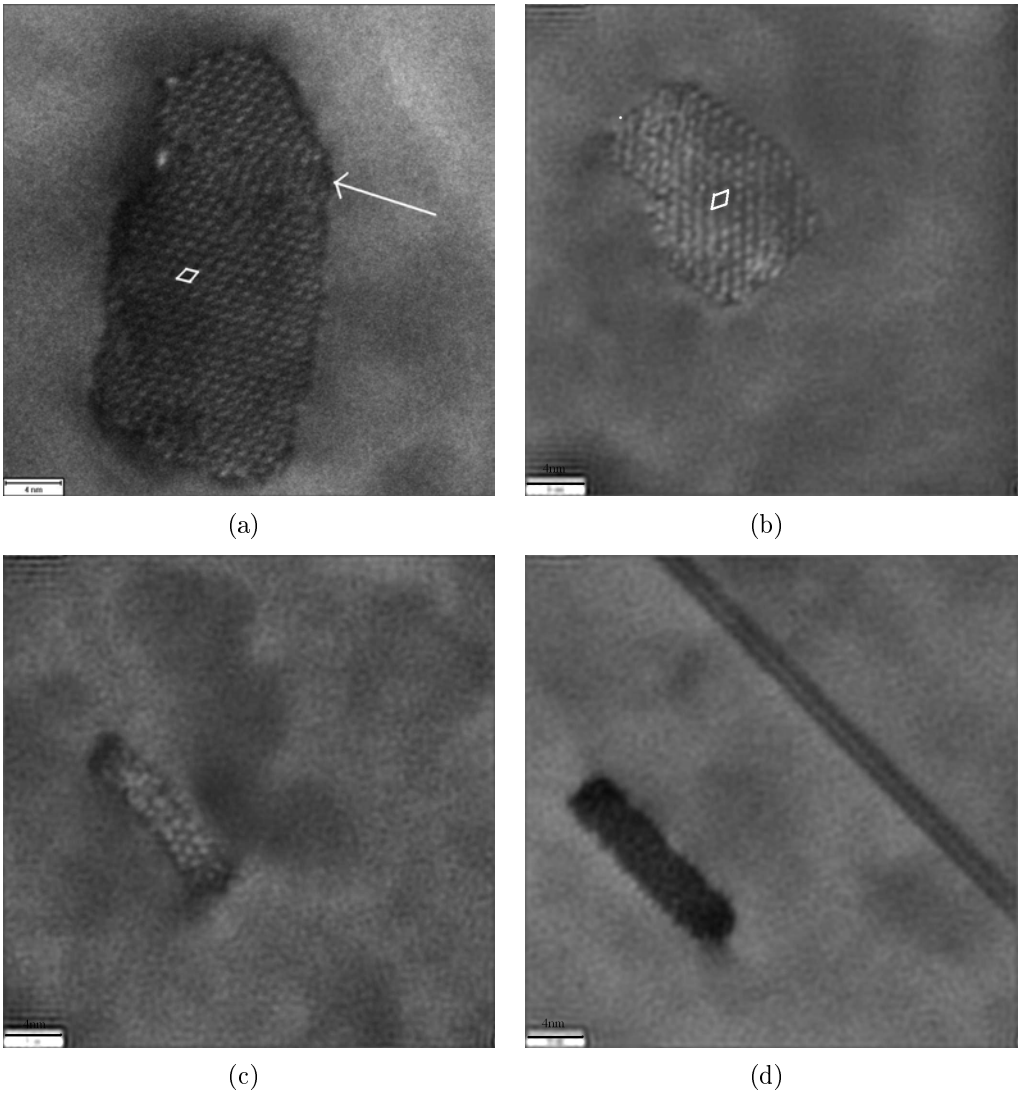

(a) (b)

(c) (d)

FIGURE 4.12. All these images are of the KKAg alloy and were taken by Calin D. Marioara. (a) This image shows a large Q-type precipitate with some disordering (Arrow) and the unit cell superimposed. (b) A Q-type precipitate with the unit cell superimposed. (c) A partially disordered platelike precipitate that is probably starting a transformation. It is partly aligned along the ⟨100⟩ and ⟨510⟩. (d) A mostly disordered platelike precipitate oriented in the ⟨100⟩-direction.

4.5.2. KKAg after heat treatment 1. In figure 4.12, some of the precipitates of the KKAg alloy is shown. Figure 4.12(a) and figure 4.12(b) shows Q-type precipitates. The periodicity here is approximately 1 *nm*. These precipitates are oriented along the ⟨510⟩-direction of aluminium. As can be seen in figure 4.7, this type of precipitate is the most common precipitate found in this alloy. Due to the low difference in the lattice constant of the Q' and the Q_{Ag}-precipitate, it has not been possible to conclude what

kind of precipitate that has formed in this alloy.

Figure 4.12(c) shows a partially transformed platelike precipitate. The lower right part is actually oriented along the ⟨510⟩-direction in aluminium, while the upper left part is oriented along the ⟨100⟩-direction. This particle has probably started the transformation into the Q-type precipitate.

A disordered platelike precipitate is shown in figure 4.12(d). This is clearly oriented along the needle shown, along the ⟨100⟩-direction. This image shows that not all the precipitates has been transformed or started to transform into the Q'-precipitate as was the case for the weaker KK4 alloy[**27**].

4.5.3. Comparison of the alloys. The KK13 alloy clearly has smaller precipitates and a higher density of precipitates than the KKAg alloy. This can be seen in figure 4.6 and 4.7. The precipitate types of these two alloys are more similar than for the KK1 and KK4 alloys investigated in my project work[**27**]. As figure 4.11 and figure 4.12 shows, both alloys have platelike precipitates as well as some Q-type precipitates.

The phase transformation has clearly progressed further in the KKAg alloy than in the KK1[**27**] and KK13 alloys. A higher number of large Q-type precipitates shows this. A larger amount of the precipitates in the KKAg alloy were oriented along the ⟨510⟩-direction, while in the KK13 alloy, most of the precipitates were oriented along the ⟨100⟩. Here, only a few precipitates could be found oriented along the ⟨510⟩-direction. In addition, more precipitates that are partially transformed were observed in this alloy than in the other two alloys. The transformation has still not gone quite as far as the transformation in the KK4 alloy had, where most of the precipitates were Q'[**27**].

4.5.4. Heat treatment 2. After heat treatment 2, the most common precipitate in all three alloys are the Q'-precipitate. In the images taken at lower magnification, some precipitates oriented along the ⟨100⟩-direction was observed, but it was not possible to get high-resolution images of any of these precipitates. The type of those precipitates is not known.

Both in figure 4.13(d) and 4.14(c) it can be seen how the precipitates nucleates of dispersoids. As seen in figure 4.8(a) and figure 4.9(a), it is quite common for the precipitates to nucleate on the dispersoids.

Figure 4.14(b) shows how the precipitate is oriented with regards to the needle along the ⟨100⟩-direction. The angle was measured to approximately 11° which is very close to the 11.3° between the ⟨510⟩-direction and the ⟨100⟩-direction. This is also true for the precipitate in figure 4.15(b). This further confirms that the Q'-precipitate has the long axis of the cross-section oriented along the ⟨510⟩-direction in aluminium.

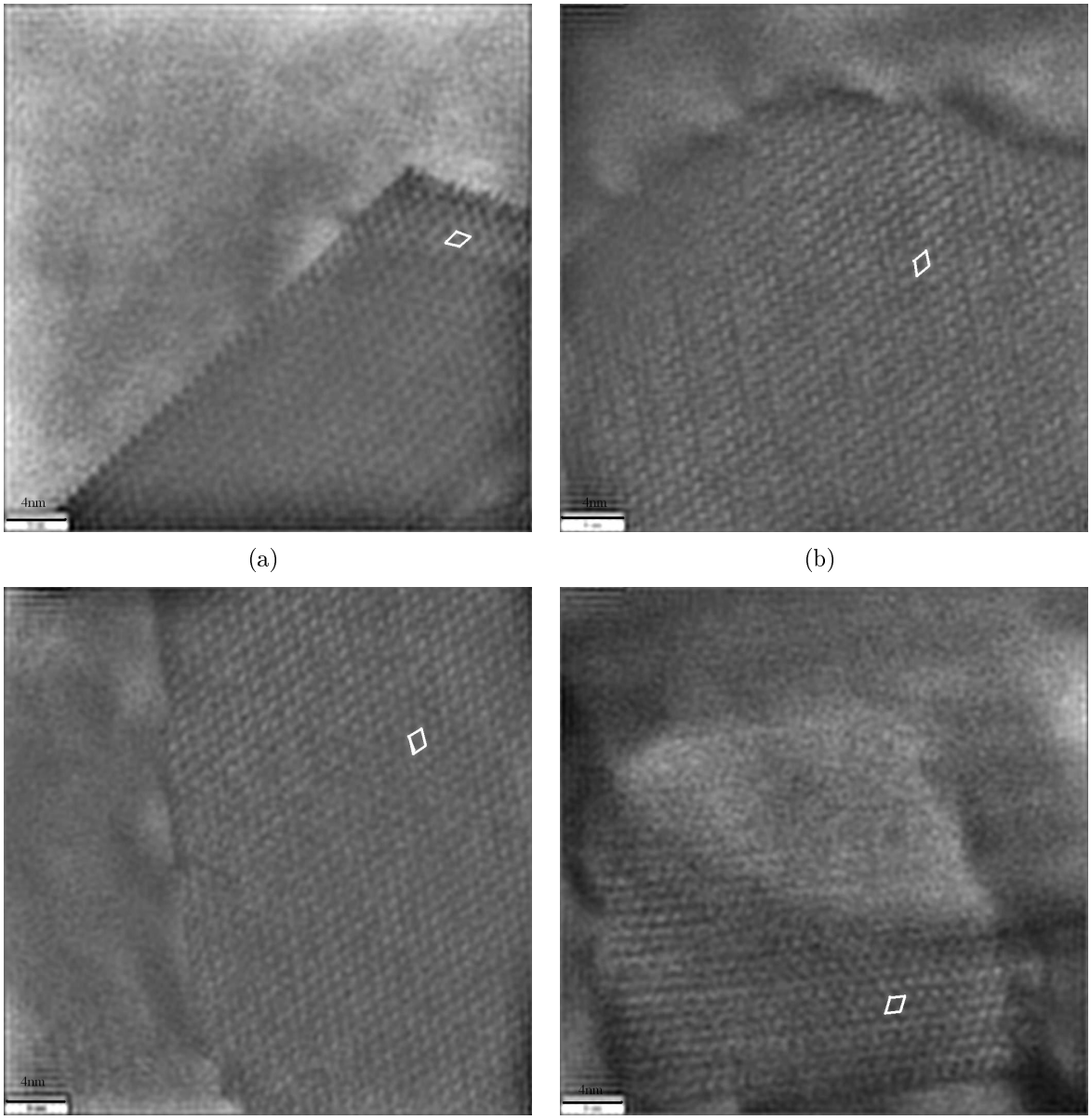

(a) (b)

(c) (d)

FIGURE 4.13. All these images are of the KK1 alloy and with unit cells superimposed. A very thin area with the correct orientation was not found in this condition. That is one of the reasons why these images are not as good as the others. (a), (b) and (c) shows large Q'-precipitates. (d) shows a Q'-precipitate that nucleates on a dispersoid. The dispersoid is in the upper part of the image.

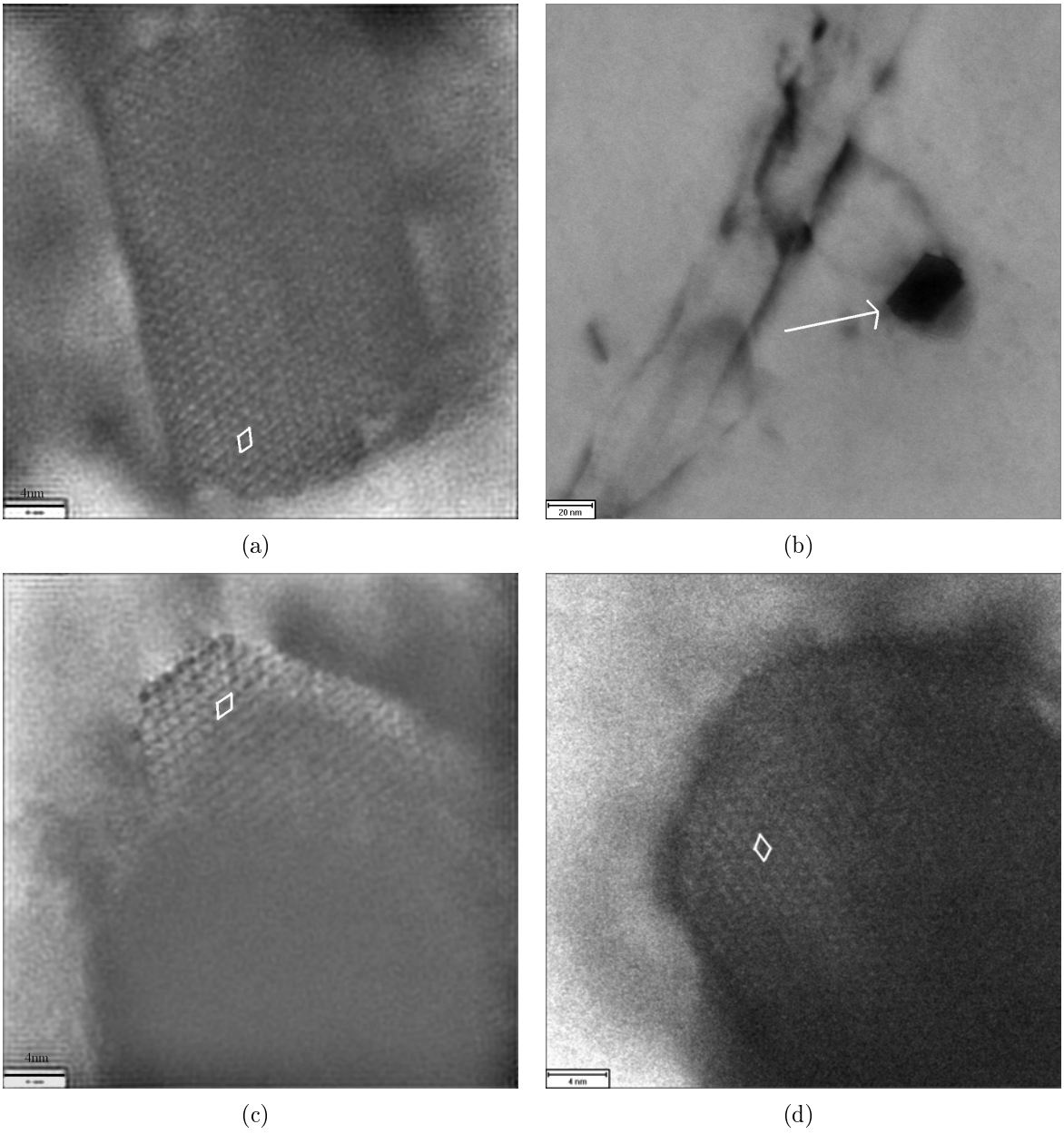

(a) (b)

(c) (d)

FIGURE 4.14. All these images are of the KK13 alloy and were taken by Calin D. Marioara. All except (b) have a unit cell superimposed. (a) and (d) shows large Q'-precipitates. (b) shows the precipitate of (a) (Arrow) together with a needle oriented along the ⟨100⟩. The precipitate is oriented along the ⟨510⟩-direction. (c) shows a Q'-precipitate nucleating on a dispersoid. (d) is dark, but some ordering can be seen.

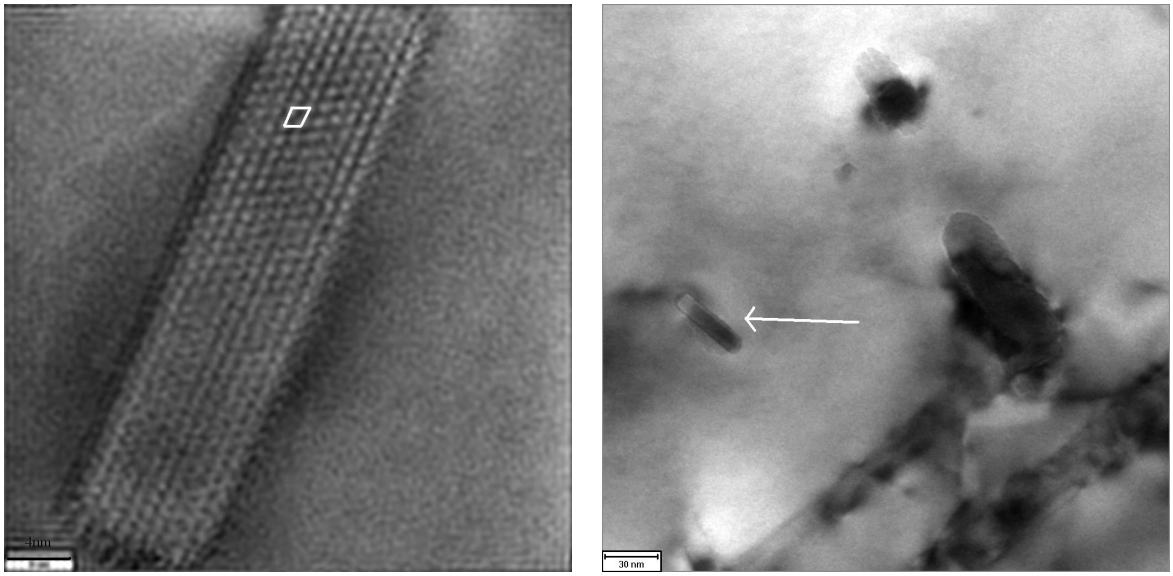

(a) (b)

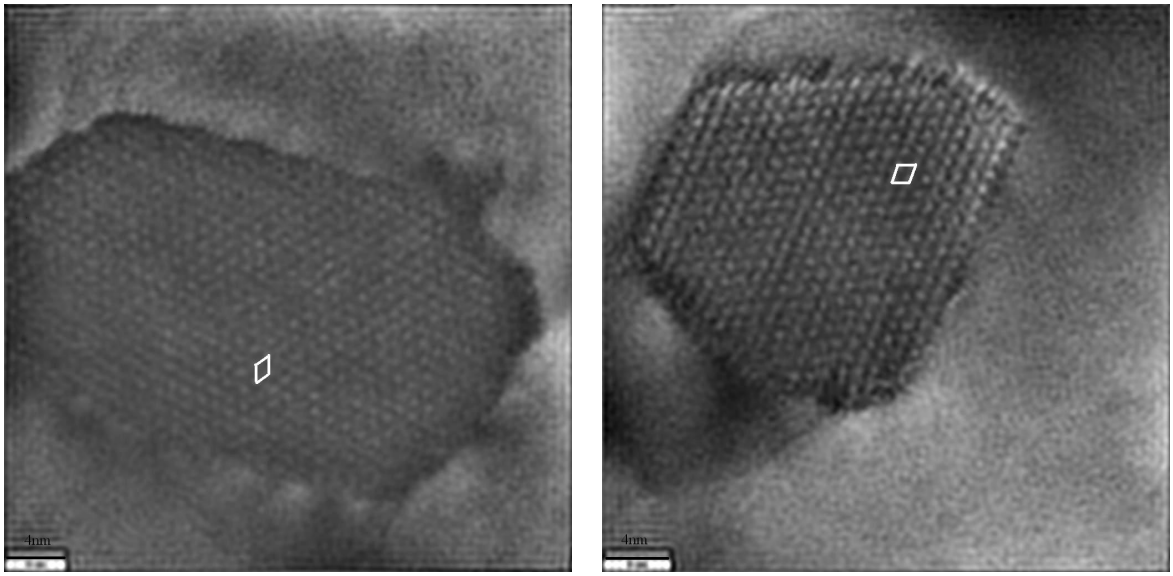

(c) (d)

FIGURE 4.15. All these images are of the KKAg alloy and were taken by Calin D. Marioara. All, except (b) have a unit cell superimposed. (a), (c) and (d) are Q'-precipitates. (b) shows the orientation of the precipitate in (a) (Arrow).

4.6. Phase identification

One of the dispersoids found in the KK1 alloy aged with heat treatment 2 was investigated to find the phase of the dispersoid. This dispersoid is shown in figure 4.17. The diameter of the dispersoid has been measured to about 130 *nm*. The compositions of both the dispersoid and the aluminium matrix are shown in table 4.4. The calculations were carried out using the EDAX software and the accuracy of these numbers is quite low. Figure 4.18(a) clearly shows a silicon peak. This means that there is some silicon in the dispersoid, but the amount of silicon is uncertain.

TABLE 4.4. The measured compositions of a dispersoid and of the aluminium matrix. It is shown both in atomic(at%) and weight(wt%) percentage.

	Mg	**Al**	**Si**	**Mn**	**Fe**	**Cu**	**O**
Dispersoid at%	0.0	56.2	0.0	13.7	1.9	17.7	10.5
Dispersoid wt%	0.0	41.4	0.0	20.5	2.9	30.6	4.6
Matrix at%	0.0	76.3	0.0	0.2	0.3	14.6	8.6
Matrix wt%	0.0	65.4	0.0	0.3	0.6	29.4	4.3

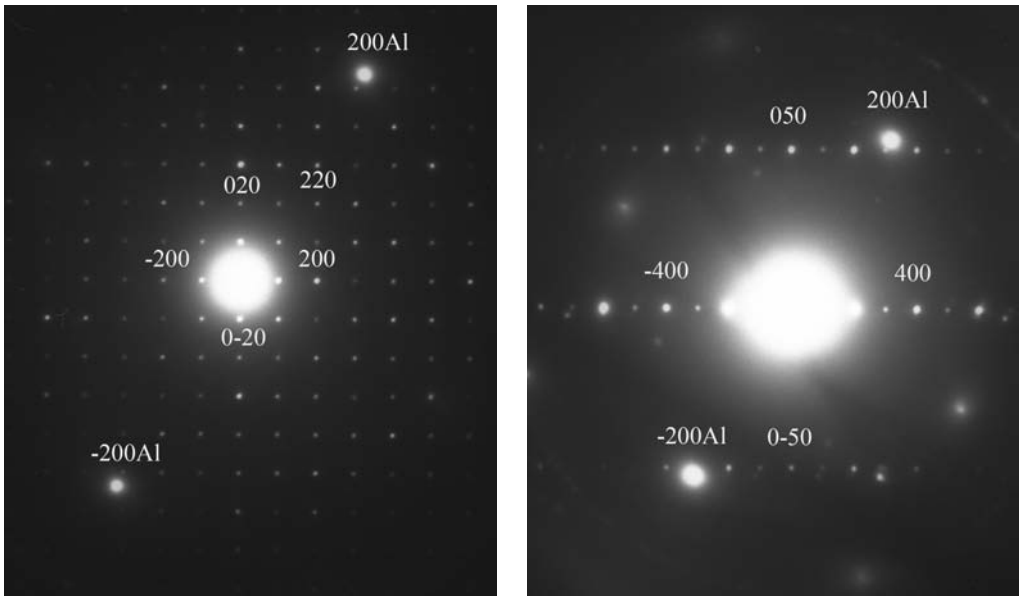

(a) (b)

FIGURE 4.16. (a) A [001]-zone axis of the dispersoid. (b) A [005]-zone axis of the dispersoid. High indexes are chosen to be avoid too much cluttering in the images. In (b) some of the spots with low indices are not seen due to the high intensity of the direct beam.

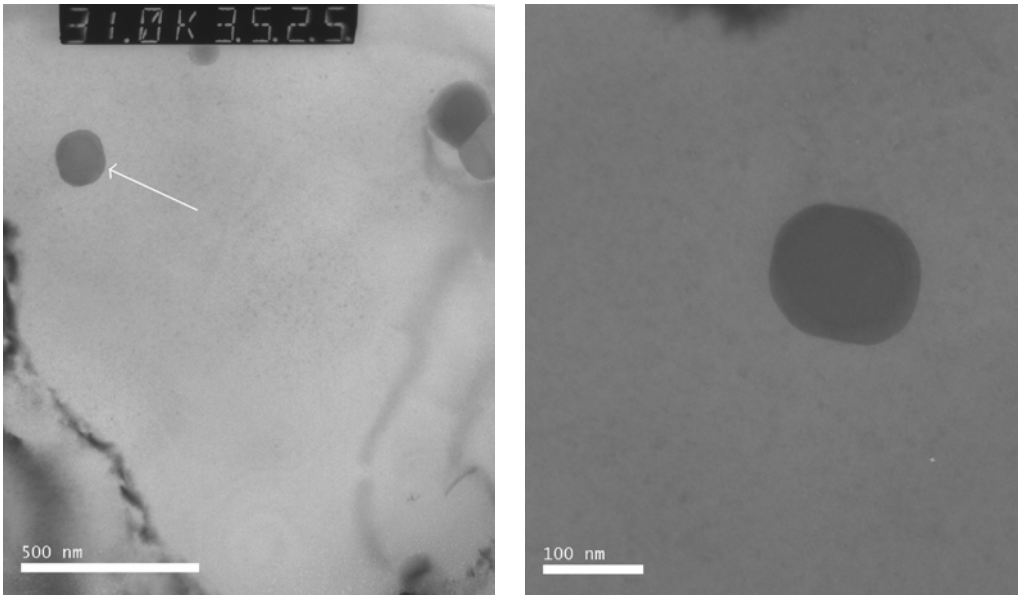

(a) (b)

FIGURE 4.17

Diffraction patterns of the dispersoid are shown in figure 4.16. Figure 4.16(a) shows the dispersoid oriented along the [100]-zone axis, while figure 4.16(b) shows the dispersoid oriented along the [500]-zone axis. The distances have been measured and the $d_{100} \approx 1.26\ nm$ and the $d_{500} \approx 0.252\ nm$. In both these figures, some reflections from the aluminium matrix is shown to ease the indexing and measurements.

Based on the measurements of the distances between the planes and the EDS-results, the dispersoid is probably of a $Al_{97-105}(Fe + Mn)_{23-24}Si_{5-11}$-type. This dispersoid has a cubic unit cell with $a = 1.256\ nm$. This fits well with the measurements. The Fe/Mn-ratio is low, approximately 0.139, which has been found to be normal for specimens after long heat treatments[**22**].

The reason for the high amount of copper found in the specimen is discussed in chapter 4.7.

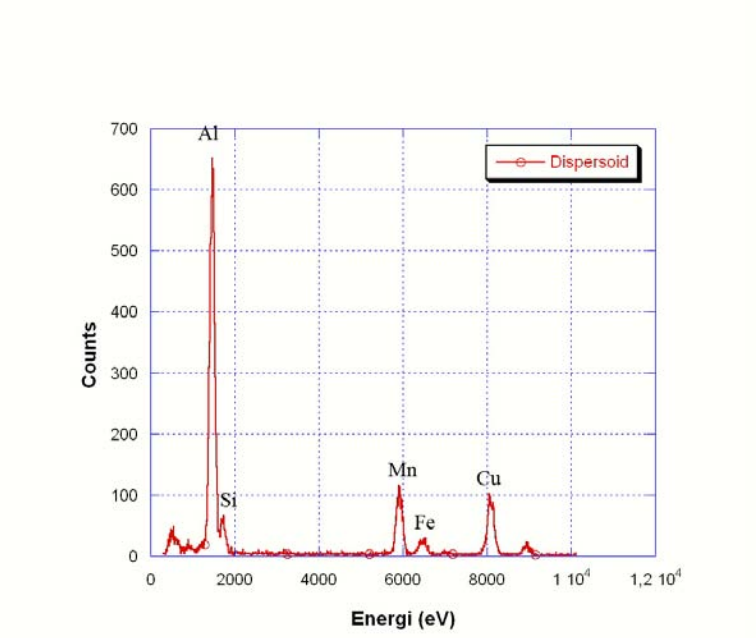

(a)

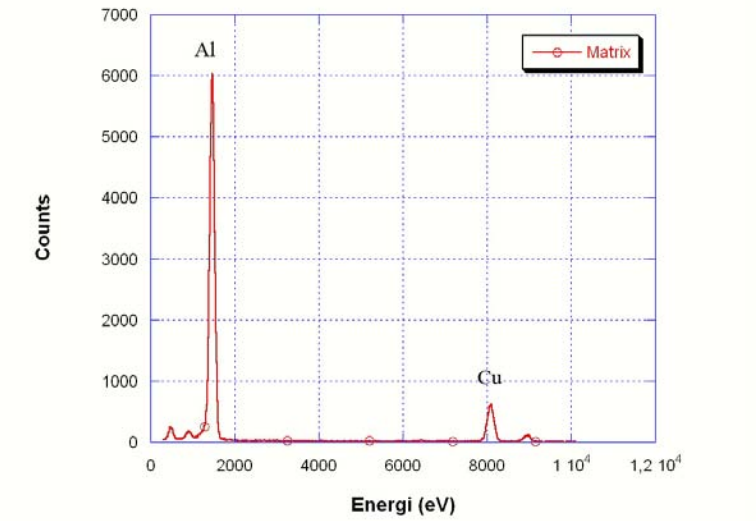

(b)

FIGURE 4.18. (a) The EDS-results of the dispersoid. (b) The EDS-results of the matrix.

4.7. Error discussions

During hardness testing, some of the indentations were not quadratic, but rather round. These were discarded, because they gave a too high hardness value. It was sometimes difficult to set the limit of how much roundness of the indentations was allowed

for it not to be discarded. This means that some of the hardness values may be slightly overestimated, but this is probably not a large error.

A problem with using TEM to investigate the microstructure of the alloys is that the TEM is not good for statistical work. If the precipitates are not spread homogeneously through the specimen, the errors will be huge. In the history of TEM, the total volume of the material analyzed approaced 0.6 mm^3[**8**]. We have assumed that the precipitation is homogeneous and in the images, the density looked to be comparable in all the areas we investigated.

The measured cross-sections varied a lot, particularly for the KKAg alloy. The cross-sections are approximated to either be circular or rectangular. Some of the cross-sections had very complicated shapes and was difficult to approximate to be either circular or rectangular. The errors in the measurements of these shapes may be significant.

The cross-sections were also sometimes difficult to distinguish from the needles, so only the clearly defined cross-sections were counted. This means that the particle density is probably underestimated.

The areas of the films were measured for each picture, but there will be some errors her as well due to the inaccuracy of the ruler used. It is estimated to 1 mm for each measurement, an error in the area of about 1.6 %. The error in the thickness measurements have been estimated to 10 %[**30**].

Accurate EDS-measurements of the precipitates and dispersoids are very difficult to get, due to the relatively small sizes of the precipitates.. The dispersoids were slightly larger and it was possible to get some results from them. A problem with these results is that with the resolution possible on the CM30 microscope, a lot of x-rays from the aluminium matrix was also measured. This makes it impossible to estimate the aluminium content of the dispersoid.

Another problem with the EDS-measurements is that the microscope has a very large copper-signal. The copper content of the dispersoid is very difficult to calculate accurately. Another problem is that both the silicon and magnesium x-ray peak is very close to the strong aluminium x-ray peak. The resolution of the system is not good enough to distinguish between these elements. The content of silicon and magnesium in the dispersoid can not be measured, even though the count graph shows a clear peak for silicon(Figure 4.18(a). The oxygen measured could be from the oxide layer on the specimen.

The lighter elements (Here: magnesium, aluminium and silicon) have characteristic x-rays with a energy that is mostly absorbed by the detector window. This means that these elements are difficult to analyze. Their characteristic x-rays are also highly absorbed in the specimen[**8**].

4.8. Future work

This is a suggestion for further work investigating these alloys. If time had allowed, several of these points would have been investigated for this Master thesis.

- Investigate the precipitates oriented along the $\langle 100 \rangle$-direction in the KK1 and KK13 alloy after 5 hours at $350°C$.
- Investigate the composition and structure of the Q-type precipitate in the KKAg alloy.
- Investigate the compositions and structures of the different dispersoids present in the alloys.
- Find how large a percentage of the total precipitation each precipitate make up.
- Investigate how long the KK13 alloy must be heat treated at $250°C$ before the precipiates are mainly Q'.

CHAPTER 5

Conclusion

- The KK13 alloy retains the hardness better than the other alloys investigated.
- The KK13 alloy is harder than the KKAg alloy due to the higher density of precipitates.
- A higher amount of the precipitates of the KKAg alloy looks to have transformed into a Q-type precipitate than in the KK13 alloy. Some transformation has taken place in both alloys.
- The hardness of all the alloys submitted to heat treatment 2 are approximately equal. It is likely they end in the same phase. The microstructure appears qualitatively to be similar.
- Almost all the precipitates in the alloys submitted to heat treatment 2 looks to be Q-type precipitates. A very few precipitates oriented along the $\langle 100 \rangle$-direction was observed.
- Much of the precipitation occurs on dispersoids and grain boundaries. It is heterogeneous.
- The dispersoid investigated has a cubic unit cell with lattice parameter $a \approx 1.26nm$. This is probably a dispersoid of the $Al_{97-105}(Fe+Mn)_{23-24}Si_{5-11}$-type.

Bibliography

[1] I. Polmear. *Light Alloys*. Elsevier, 4 edition, 2006.

[2] J.D. Verhoeven. *Fundamentals of physical Metallurgy*. Wiley, 1975.

[3] Statistisk sentralbyrå. http://www.ssb.no/uhaar/tab-21.html.

[4] Statistisk Sentralbyrå. http://www.ssb.no/uhaar/tab-03.html.

[5] E.J. Samuelsen. *Materials physics*. NTNU Trykk, 2006.

[6] G. Strobl. *Condensed Matter Physics*. Springer, 2004.

[7] S. Elliot. *The Physics and Chemistry of Solids*. Wiley, 1998.

[8] C.B. Carter D.B. Williams. *Transmission Electron Microscopy*. Springer, 1996.

[9] P. Hirsch et al. *Electron Microscopy of thin crystals*. Robert E. Krieger, 1977.

[10] B. Thundal. *Aluminium*. Almqvist & Wiksell, 1991.

[11] C.D. Marioara et al. The effect of cu on precipitation al-mg-si alloys. *Phil. Mag.*, 87(23):3385 –3413, 2007.

[12] S.J. Andersen et al. The crystal structure of the β" phase in al-mg-si alloys. *Acta Mater*, 46(9):3283–3298, 1998.

[13] J. Jansen et al. C.D. Marioara, S.J. Andersen. The influence of temperature and storage time at rt on nucleation of the β" phase in a 6082 al-mg-si alloy. *Acta Mater*, 51:789–796, 2003.

[14] S.J. Andersen et al. C.D. Marioara. The influence of alloy composition on precipitates of the al-mg-si system. *Metallurgical and materials transactions*, 36A:691–702, 2005.

[15] ICAA. *Crystal structure determination of the Q' and C-type plate precipitates in Al-Mg-Si-Cu (6xxx) alloys*, 2008. ICAA 2008 conference poster.

[16] A. Gaber et al. Dsc and hrtem investigation of the precipitates in $al - 1.0\%mg_2si - 0.5\%agalloy$. *Materials Science and Technology*, 20:1627–1631, 2004.

[17] K. Matsuda et al. A. Furihata. Age-hardening behavior and hrtem observation of precipitates in excess mg type al-mg-si-ag alloy. *Mat. Sci. Forum*, 519-521:507–510, 2006.

[18] K. Matsuda et al. New quaternary grain boundary precipitate in al-mg-si alloy containing silver. *Scripta Materialia*, 55:127–129, 2006.

[19] J. Nakamura et al. The effect of ag-addition on crystal structure of β'-phase in al-mg-si alloy. *Materials Science Forum*, 519-521:511–514, 2006.

[20] A.L. Dons. Sintef. Unpublished results.

[21] C.D. Marioara. Oral and written discussions with C.D. Marioara.

[22] Y. Wu et al. The microstructure evolution of an al-mg-si-mn-cu-ce alloy during homogenization. *Journal of Alloys and Compounds*, 475:332–338, 2009.

[23] W. Eidhed et al. Effects of homogenisation conditions on semisolid microstructures of al-mg-si-mn alloys produced by d-ssf process. *International Journal of Cast Metals Research*, 21(1-4):168–173, 2008.

[24] D. H. Lee et al. Enhancement of mechanical properties of al-mg-si alloys by means of manganese dispersoids. *Materials Science and Technology*, 15:450–455, 1999.

[25] ISO International organization for standardization. *Metallic materials, Vickers hardness test Part 1: Test method*. Norsk Standardiseringsforbund, 1997. ISO 6507-1:1997.

[26] D.J. Griffiths. *Introduction to Electrodynamics*. Prentice Hall, 3 edition, 1999.

[27] J. Holmestad. High-temperature stability of al-mg-si-cu alloys. Master's thesis, NTNU, 2008.

[28] I.J. Polmear. Effects of small additions of silver on aging of some aluminum alloys. *Trans. Met. Soc.*, page 1331, 1964.
[29] TEM Gemini center. http://home.phys.ntnu.no/brukdef/prosjekter/gemini/index.php?mw=main.
[30] B. Holme C.D. Marioara, S.J. Andersen. Methodology for quantification of needle precipitates in 6xxx al-mg-si(-cu) alloys. Presentation.
[31] H. Nordmark. Tem studies of the phase transformation β" - β'/u in al-mg-si alloys. Master's thesis, NTNU, 2003.

APPENDIX A

Tables

TABLE A.1. The Vickers hardness values for each alloy.

Time (h)	**KK11** HV5	**KK13** HV5	**KK14** HV5	**KK15** HV5	**KKAg** HV5
0	118.7 ± 1.30	120.5 ± 1.08	125.7 ± 0.67	120.1 ± 0.74	125.5 ± 1.11
0.25	119.3 ± 0.76	117.7 ± 0.79	121.0 ± 1.10	117.7 ± 0.97	123.6 ± 0.88
0.5	118.2 ± 0.81	114.6 ± 0.43	123.2 ± 1.15	113.7 ± 0.68	122.2 ± 0.66
1	113.5 ± 0.65	114.5 ± 0.99	118.8 ± 1.04	108.4 ± 0.78	120.2 ± 1.40
1.5	109.7 ± 0.93	111.3 ± 1.19	113.7 ± 0.83	105.0 ± 0.88	114.8 ± 1.40
2	104.6 ± 0.95	112.1 ± 0.62	112.9 ± 0.94	103.4 ± 0.64	111.2 ± 0.98
2.5	104.1 ± 0.67	111.3 ± 0.84	111.0 ± 0.92	98.1 ± 1.11	110.7 ± 0.72
3	101.6 ± 1.81	109.3 ± 0.60	110.2 ± 0.49	101.8 ± 0.57	107.7 ± 0.96
4	97.7 ± 0.50	103.7 ± 0.47	102.5 ± 0.67	95.5 ± 0.72	101.6 ± 1.53
5	98.4 ± 0.91	105.3 ± 0.86	101.6 ± 0.90	96.2 ± 0.47	100.7 ± 1.45
7	92.8 ± 0.71	102.7 ± 0.63	100.7 ± 1.02	91.3 ± 0.62	97.8 ± 0.92
10	91.2 ± 0.66	99.0 ± 0.87	97.6 ± 0.83	90.9 ± 0.59	96.1 ± 1.10
15	86.6 ± 0.64	97.6 ± 1.07	97.6 ± 0.97	88.9 ± 0.50	94.1 ± 0.60
24	82.9 ± 0.46	91.7 ± 0.98	94.1 ± 0.55	84.2 ± 0.65	90.7 ± 0.54
36	75.1 ± 1.10	87.5 ± 1.34	87.6 ± 0.96	79.1 ± 0.96	86.4 ± 1.08
48	72.9 ± 0.38	85.4 ± 1.03	83.7 ± 0.47	75.7 ± 0.84	79.8 ± 1.58
60	71.9 ± 0.55	$81. \pm 0.65$	80.6 ± 0.60	72.1 ± 0.43	78.0 ± 0.73
72	70.7 ± 0.37	80.0 ± 1.25	78.3 ± 0.52	72.5 ± 0.56	77.6 ± 0.81
100	65.9 ± 0.62	78.4 ± 1.66	77.1 ± 0.53	69.5 ± 0.50	72.4 ± 0.95

APPENDIX B

TEM images

B.1. KK13 images used for needle length and number density

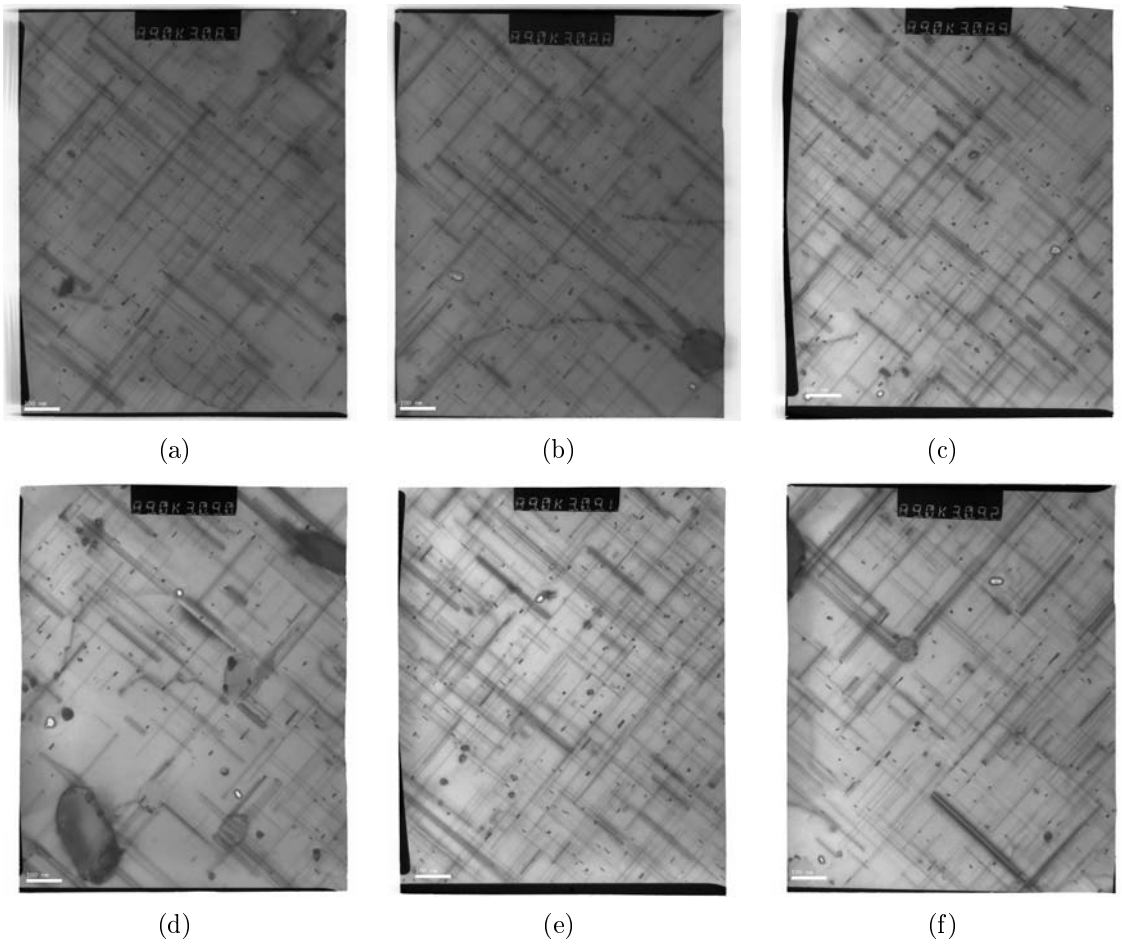

(a) (b) (c)

(d) (e) (f)

FIGURE B.1. The images used for number density and needle length measurements of the KK13 alloy, all taken by Calin D. Marioara.

B.2. Images of KK13 used for cross-section meausurements

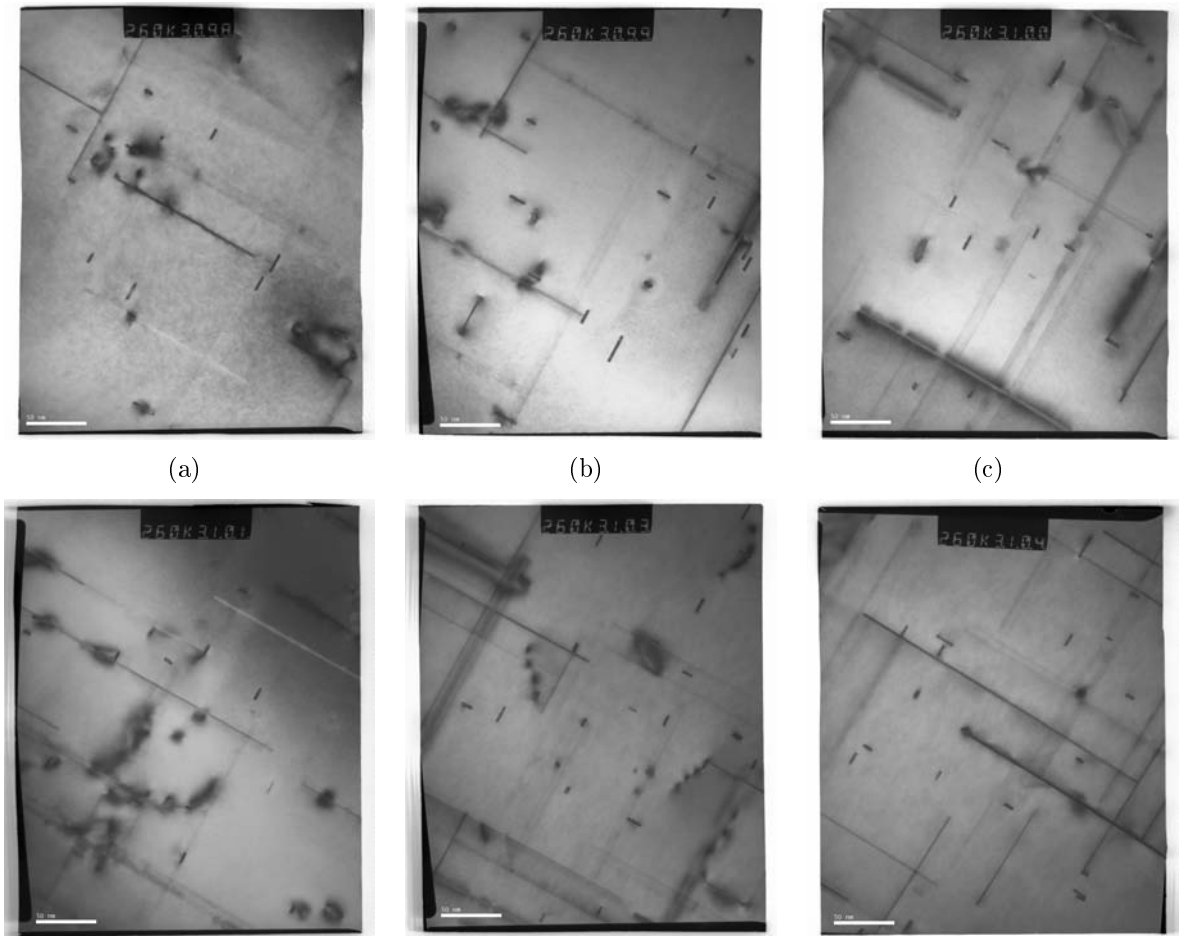

(a) (b) (c)

(d) (e) (f)

FIGURE B.2. The images used for cross-section measurements of the KK13 alloy, all taken by Calin D. Marioara.

B.3. KKAg images used for needle length and number density

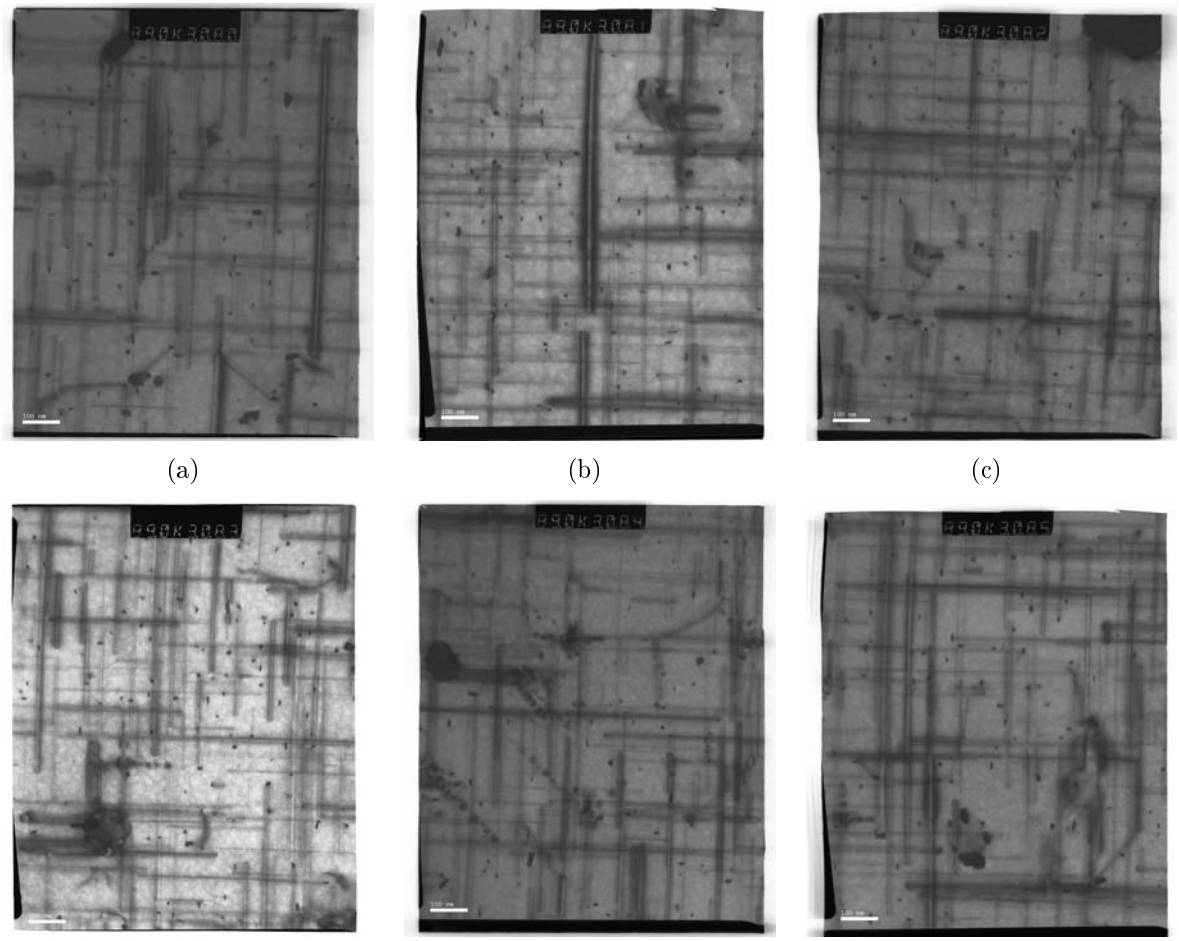

(a) (b) (c)

(d) (e) (f)

FIGURE B.3. The images used for number density measurements of the KKAg alloy, all taken by Calin D. Marioara.

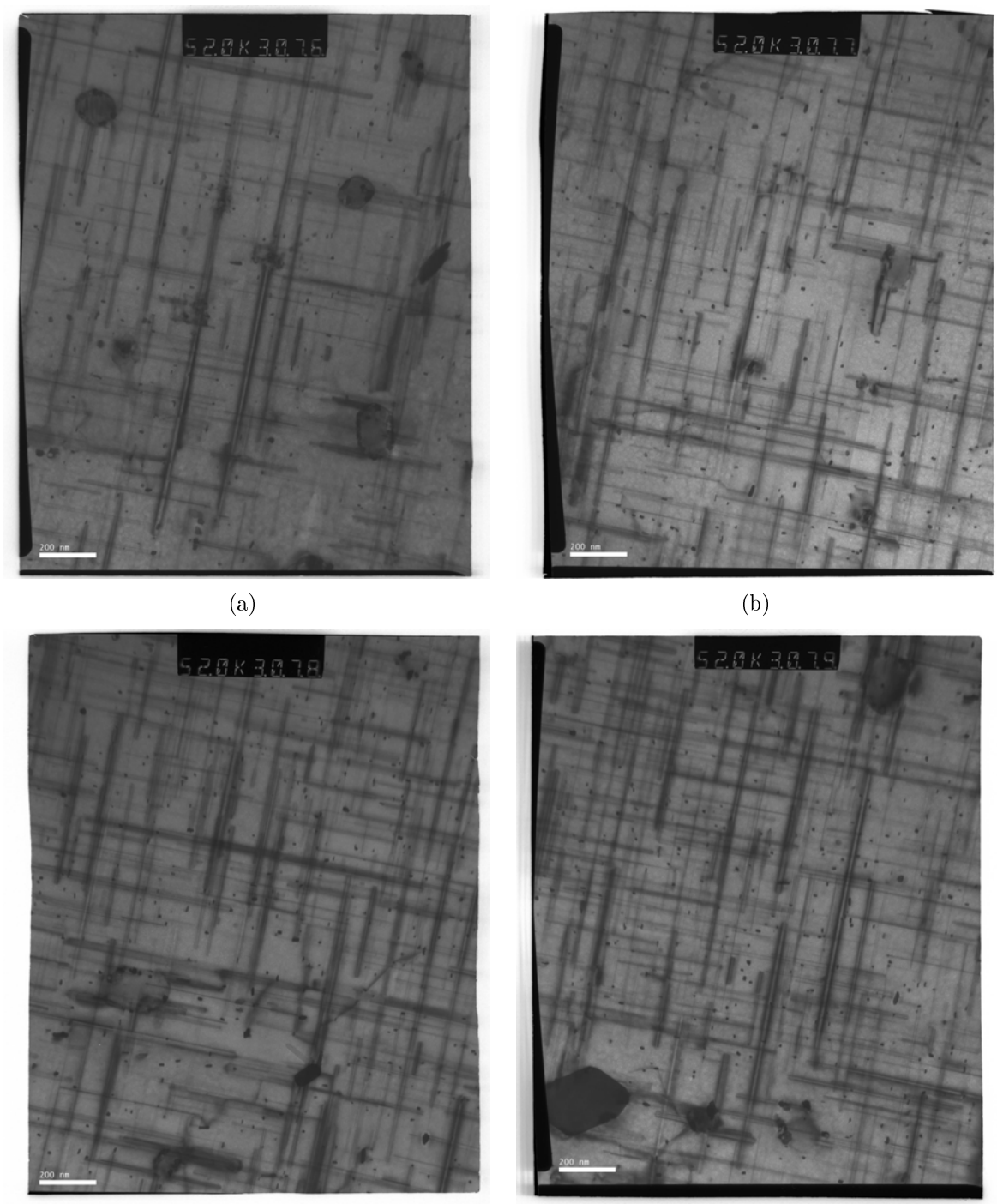

FIGURE B.4. The images used for needle length measurements of the KKAg alloy, all taken by Calin D. Marioara.

B.4. Images of KKAg used for cross-section meausurements

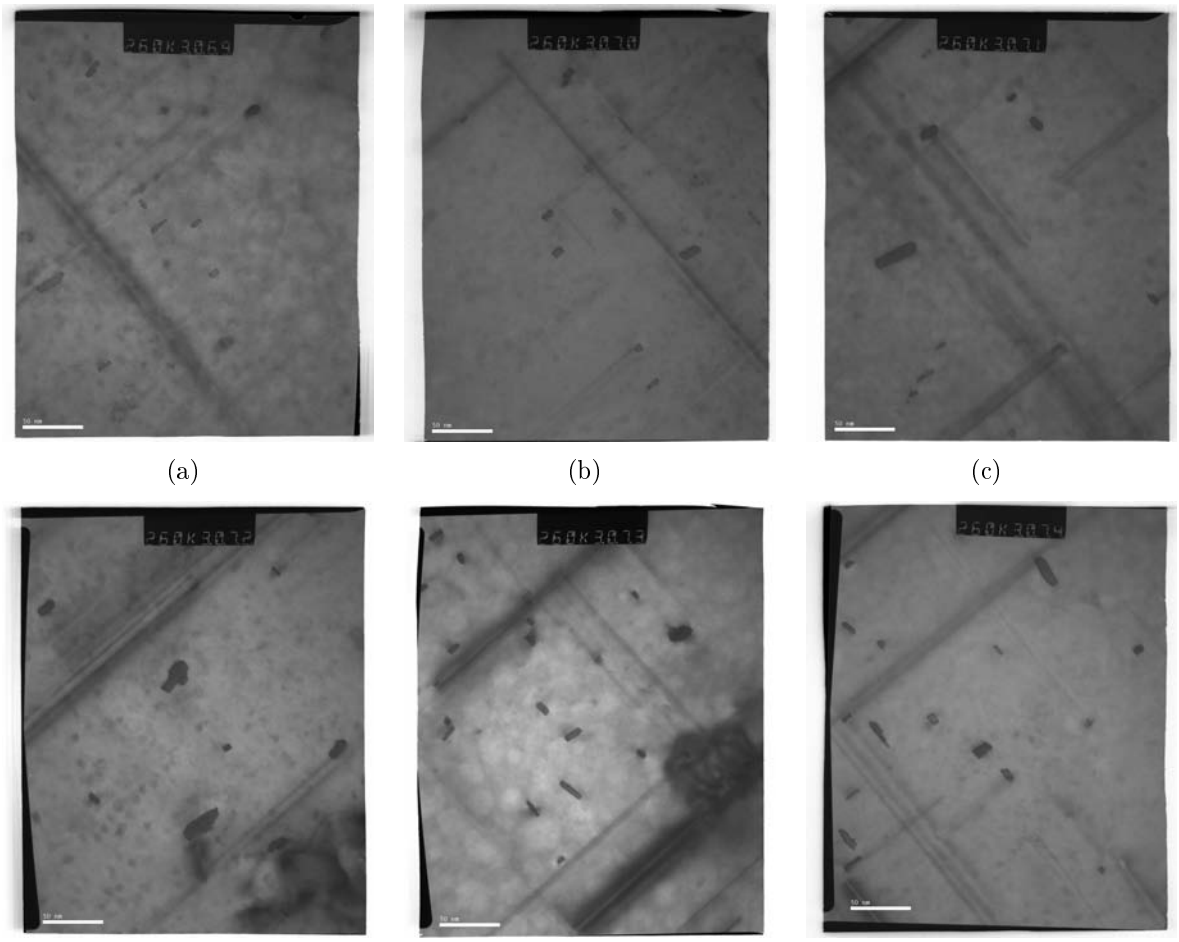

(a) (b) (c)

(d) (e) (f)

FIGURE B.5. The images used for cross-section measurements of the KKAg alloy, all taken by Calin D. Marioara.